Rheological Transitions Facilitate Fault-Spanning Ruptures on Seismically Active and Creeping Faults

Martijn P.A. van den Ende, J. Chen, A. Niemeijer, J.-p. Ampuero

AGU ADVANCING EARTH AND SPACE SCIENCE

JGR Solid Earth

RESEARCH ARTICLE
10.1029/2019JB019328

Key Points:
- Physically based seismic cycle simulations are performed, incorporating fault zone structure and composition
- Both seismogenic and predominantly creeping faults are observed to generate large seismic events
- The nucleation of giant earthquakes on creeping faults is facilitated by rheological transitions

Correspondence to:
M. P. A. van den Ende,
martijn.vandenende@geoazur.unice.fr

Citation:
van den Ende, M. P. A., Chen, J., Niemeijer, A. R., & Ampuero, J.-P. (2020). Rheological transitions facilitate fault-spanning ruptures on seismically active and creeping faults. *Journal of Geophysical Research: Solid Earth*, *125*, e2019JB019328. https://doi.org/10.1029/2019JB019328

Received 31 DEC 2019
Accepted 11 JUN 2020
Accepted article online 24 JUN 2020

Rheological Transitions Facilitate Fault-Spanning Ruptures on Seismically Active and Creeping Faults

M. P. A. van den Ende[1,2], J. Chen[2,3], A. R. Niemeijer[2], and J.-P. Ampuero[1,4]

[1]Université Côte d'Azur, IRD, CNRS, Observatoire de la Côte d'Azur, Géoazur, Valbonne, France, [2]High Pressure and Temperature Laboratory, Department of Earth Sciences, Utrecht University, The Netherlands, [3]Now at Geoscience and Engineering Department, Delft University of Technology, Delft, The Netherlands, [4]Seismological Laboratory, California Institute of Technology, Pasadena, CA, USA

Abstract Physical constraints on the seismogenic potential of major fault zones may aid in improving seismic hazard assessments, but the mechanics of earthquake nucleation and rupture are obscured by the complexity that faults display. In this work, we investigate the mechanisms behind giant earthquakes by employing a microphysically based seismic cycle simulator. This microphysical approach is directly based on the mechanics of friction as inferred from laboratory tests and can explain a broad spectrum of fault slip behavior. We show that regular earthquakes are controlled by the size and distribution of (nominally) frictionally unstable asperities, whereas fault-spanning earthquakes are governed by a rheological transition occurring in creeping fault segments. Moreover, this facilitates the nucleation of giant earthquakes on faults that are weakly seismically coupled (i.e., creeping). This microphysically based approach offers opportunities for investigating long-term seismic cycle behavior of natural faults.

1. Introduction

One major limitation of seismic hazard assessments is that they are mostly based on statistics rather than physics. Particularly for large earthquakes that have recurrence times of up to several centuries, instrumental catalogues of seismic events in a given region are short or absent, so that statistical analyses can only be performed through the extrapolation of smaller, more frequent events, which entails model assumptions that are difficult to test. Constraints originating from a physical understanding of earthquakes may therefore greatly improve seismic hazard assessments, but basic underlying mechanisms are obscured by the enormous complexity inherent to natural fault zones.

Over the last two decades or so, innovative techniques in paleoseismology have substantially expanded our catalogue of (pre)historic seismic events, revealing earthquake supercycles in the form of spatiotemporal clustering of earthquakes (Benedetti et al., 2013; Philibosian et al., 2017; Ratzov et al., 2015; Sieh et al., 2008) and occurrences of exceptionally large events ("superimposed cycles") (Goldfinger et al., 2012, 2013; Mannen et al., 2018; Satake, 2015). In addition, millenary recurrence of $M_w \geq 9.0$ earthquakes has been anticipated for the Main Himalayan Thrust (Stevens & Avouac, 2016) and Japan Trench (Satake & Fujii, 2014) regions on the basis of geodetic estimates of moment accumulation rates. These inferences suggest that the lack of instrumental recordings of great ($M_w > 8$) and giant ($M_w > 9$) earthquakes does not imply an intrinsic upper limit of event magnitude. The 2004 Sumatra-Andaman and 2011 Tohoku-Oki $M_w > 9$ events, hosted by subduction thrusts that were previously marked in hazard maps as being incapable of generating such large magnitude events (Ruff & Kanamori, 1980; Satake & Atwater, 2007; Satake & Fujii, 2014), are exemplary to this notion. Statistical analyses of earthquake catalogues do not exclude that most subduction regions are intrinsically capable of hosting giant earthquakes (Kagan, 1997; McCaffrey, 2008), provided that the seismogenic zone geometry is not restrictive (e.g., Weng & Yang, 2017).

The occurrence of great earthquakes in all subduction settings is suggestive of a common underlying mechanism. On the other hand, though numerous subduction regions have been identified to host giant earthquakes, some of these regions presently exhibit high seismicity rates, such as the Japan Trench (Satake, 2015) and Sumatra (Sieh et al., 2008), while other megathrusts are currently quiescent except for deeper slow slip and tremor (Alaska, Cascadia; Gomberg, 2010; Ohta et al., 2006) or generally display low

levels of background seismicity (Andaman, Chile Maule; Ide, 2013). This geographical variability in seismic character requires that the mechanism for the generation of giant earthquakes be at least partly independent of that of regular earthquakes, allowing great and giant earthquakes to occur in both seismically active and quiet regions (where "quiet" is defined in the context of producing only few earthquakes of small or moderate size). Furthermore, seismological and numerical evidence suggests that creeping (weakly seismically coupled) fault segments may facilitate propagation of dynamic ruptures (Bécel et al., 2017; Noda & Lapusta 2013; Witter et al., 2016), even though creeping segments are generally thought to impede fast rupture events (Kaneko et al., 2010). To elucidate the emergence of giant earthquakes that inevitably propagate through (or possibly nucleate within) creeping fault segments, the underlying physical mechanisms of fault rock deformation need to be closely considered.

In this work, we numerically examine the behavior of compositionally heterogeneous faults and investigate the mechanisms behind giant earthquakes from a microphysical standpoint. To this end, we employ the *Chen-Niemeijer-Spiers* (CNS) microphysical model (Chen & Spiers, 2016; Niemeijer & Spiers, 2007) as implemented into the QDYN seismic cycle simulator (Luo et al., 2017; van den Ende, Chen, et al., 2018) that enables us to simulate numerous earthquake cycles, using a fault rheology motivated by field geological observations. We subsequently discuss the micromechanics of earthquakes that traverse through or nucleate in fault regions that are unfavorable for unstable slip, hence facilitating fault-spanning earthquake ruptures. We conclude by placing these results into a broader context of earthquake forecasting, enabled by physical considerations.

2. Methods

2.1. Geology of a Subduction Thrust Interface

In characterizing a typical fault zone structure, the Punchbowl fault (Chester & Logan, 1987; Chester et al., 1993) is commonly taken as a model for mature crustal faults. However, fault core architectures may strongly vary under influence of the protolith (Bullock et al., 2014; Faulkner et al., 2010): faults cross-cutting predominant quartzo-feldspathic, carbonaceous, or crystalline lithologies often accommodate strain within a single, straight, and narrow fault core, no more than a few meters in width, surrounded by a damage zone (Chester et al., 1993; De Paola et al., 2008; Faulkner et al., 2010; Fondriest et al., 2012). Shear strain within the fault core itself is typically localized in millimeter to centimeter wide principal slip zones, with an additional hierarchical level of localization (the principal slip surface) at the micrometer scale.

Conversely, phyllosilicate-bearing or mixed lithology fault zones are characterized by multiple fault cores, spatially distributed within up to a kilometer-wide zone (Faulkner et al., 2003; Jefferies et al., 2006; Rowe et al., 2011). Exhumed tectonic mélanges feature boudinaged lenses of competent material (such as dolomite, quartz, chert, or basalt) embedded in a less-competent, phyllosilicate-rich matrix, enclosed or cross-cut by a number of undulating fault strands (Collettini et al., 2011; Fagereng, 2011b; Faulkner et al., 2003; Kimura et al., 2012; Niemeijer & Collettini, 2014; Rowe et al., 2011)—see Figure 1a. The phyllonite matrix typically displays distributed deformation with a pervasive, well-developed foliation and abundant pressure solution seams, suggesting that pressure solution is a dominant deformation mechanism (Fagereng, 2011b; Kimura et al., 2012). By contrast, thin (millimeter- to centimeter-thick) layers of gouge or ultracataclasite bounding the competent lenses evidence localized deformation (Faulkner et al., 2003; Kimura et al., 2012). The numerous cataclastic features (grain comminution, fracturing, polished and striated surfaces) hosted within the localized slip zones and competent blocks are accompanied by evident dissolution/precipitation textures, indicating that pressure solution occurs broadly contemporaneously with granular flow over the course of a seismic cycle (Bullock et al., 2014; Hadizadeh et al., 2012; Holdsworth et al., 2011; Jefferies et al., 2006; Smeraglia et al., 2017, and others). The interplay between these two mechanisms (granular flow and pressure solution) forms the basis of the Chen-Niemeijer-Spiers microphysical model adopted for this study, and these field observations can be readily incorporated into the simulations.

2.2. Model Rheology and Constitutive Relations

The derivation of the CNS model, the comparison with classical rate-and-state friction, and its implementation into QDYN are described in detail in Chen and Spiers (2016), Chen and Niemeijer (2017), Chen,

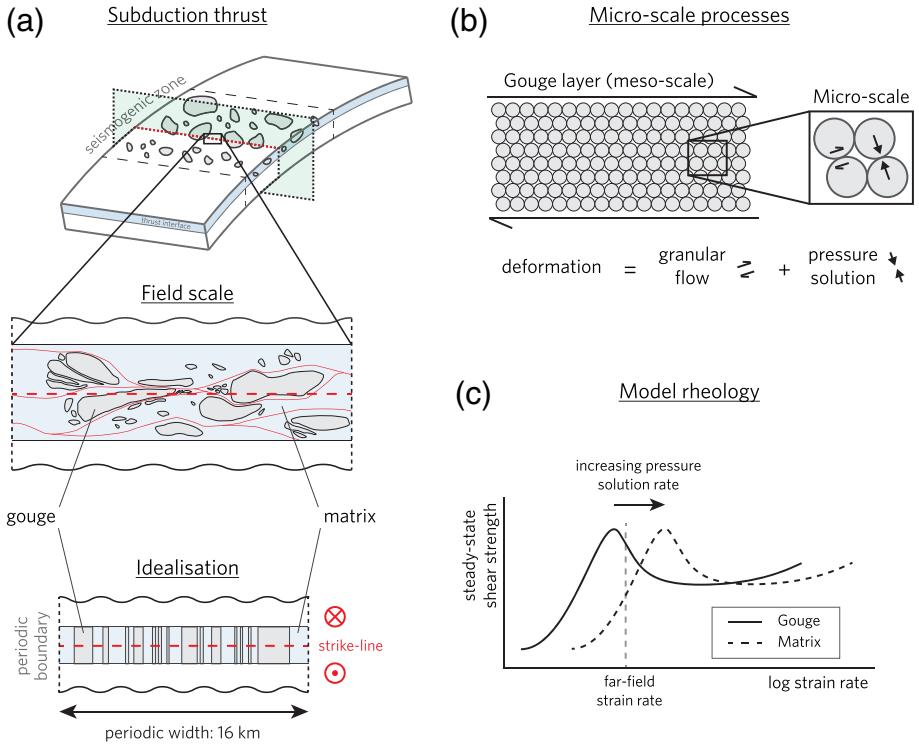

Figure 1. Synoptic overview of the properties of the model fault. (a) Idealization of the envisioned fault geometry, after Fagereng (2011b). The compositional heterogeneity on the subduction interface is represented by an alternating sequence of nominally stable and unstable fault patches. (b) Assumed microstructure and microprocesses (granular flow and pressure solution) that operate in parallel to accommodate the imposed strain rate. (c) Schematic diagram of the steady-state shear strength versus strain rate, as predicted by the CNS microphysical model. The compositional variation along the fault is reflected by a contrast in pressure solution kinetics, causing a relative shift of the steady-state strength curves.

Niemeijer, and Spiers (2017), Niemeijer and Spiers (2007), and van den Ende, Chen, et al. (2018). Some key concepts of this model are recited here.

The CNS model geometry is based on the microstructural observations provided by Niemeijer and Spiers (2006) and considers a granular gouge layer of uniform thickness h, characterized by a nominal grain size d and porosity ϕ. A representative volume element is subjected to an effective normal stress σ and deformation rate V_{imp}, which is accommodated internally by parallel operation of granular flow (grain rolling and sliding), and one or more thermally activated, time-dependent deformation mechanisms (Figure 1b). Following previous work (Chen & Spiers, 2016; Niemeijer & Spiers, 2007; van den Ende, Chen, et al. 2018) and based on the observations summarized in section 2.1, we take intergranular pressure solution as the sole time-dependent mechanism, ignoring other mechanisms such as stress corrosion cracking (Atkinson, 1984; Brantut et al., 2013). The constitutive relation for the rheology of the fault then results from the individual constitutive relations for granular flow and pressure solution, which are dependent on the instantaneous state of stress and gouge porosity. While other deformation mechanisms may occur at similar rates, in this study, we limit ourselves to pressure solution creep to facilitate comparison with previous laboratory and numerical studies that focused on this mechanism.

For intergranular pressure solution, the flow law for dissolution controlled pressure solution creep is given as

$$\dot{\gamma}_{ps} = Z_{ps}\tau f_1(\phi) \tag{1a}$$

$$\dot{\varepsilon}_{ps} = Z_{ps}\sigma f_2(\phi) \tag{1b}$$

Here, $\dot{\gamma}_{ps}$ and $\dot{\varepsilon}_{ps}$ are the strain rates in the fault tangential and normal directions, respectively. These are proportional to the macroscopic shear stress (τ) and effective normal stress (σ) through the

temperature-dependent pressure solution kinetics (Z_{ps}). This kinetic parameter can be computed based on the gouge nominal grain size, ambient temperature, and grain geometry (see Niemeijer et al., 2002; Pluymakers et al., 2014), but which we combine into one parameter for simplicity. The evolution of the grain-grain contact area (and grain contact stress) with porosity ϕ is described by the porosity function $f_i(\phi)$ (Spiers et al., 2004). For dissolution controlled pressure solution creep, this function takes the following form (Pluymakers et al., 2014; van den Ende, Chen, et al., 2018):

$$f_1(\phi) = \frac{\phi_c}{\phi_c - \phi} \tag{2a}$$

$$f_2(\phi) = \frac{\phi - \phi_0}{\phi_c - \phi} \tag{2b}$$

where ϕ_0 is a lower cutoff porosity corresponding to the percolation threshold for an interconnected pore network of 3% (van der Marck, 1996) and ϕ_c is the maximum attainable porosity of a purely dilatant gouge material, referred to here as the "critical state" porosity (Niemeijer & Spiers, 2007; Paterson, 1995). Typically, a porosity function similar to $f_1(\phi)$ is used in analytical models for intergranular pressure solution that employ a porosity function (Pluymakers et al., 2014; Spiers et al., 2004). However, in laboratory compaction test, it has been observed that microphysical model predictions for compaction by pressure solution overestimate experimentally measured strain rates at low porosities (<20%), sometimes by several orders of magnitude (Niemeijer et al., 2002). While the physical mechanisms behind this discrepancy are yet to be fully identified (e.g., van den Ende et al., 2019), the trends in the experimental data can be approximated by the modified porosity function $f_2(\phi)$, which asymptotically reduces $\dot{\varepsilon}_{ps}$ to zero for $\phi \rightarrow \phi_0$. Furthermore, this ensures that $\phi > \phi_0$ at all times, preventing negative porosities that are physically unrealistic. By contrast, shear creep accommodated by pressure solution does not involve volume changes (i.e., porosity reduction), so it is expected that $\dot{\gamma}_{ps} > 0$ even for $\phi = \phi_0$ (e.g., Bos et al., 2000). A functional form like $f_1(\phi)$ is therefore more likely to describe shear creep by pressure solution, as is adopted for this study.

The constitutive relations for granular flow have been derived as (Chen & Spiers, 2016)

$$\dot{\gamma}_{gr} = \dot{\gamma}^*_{gr} \exp\left(\frac{\tau[1 - \tilde{\mu}^* \tan\psi] - \sigma[\tilde{\mu}^* + \tan\psi]}{\tilde{a}[\sigma + \tau \tan\psi]}\right) \tag{3a}$$

$$\dot{\varepsilon}_{gr} = -\tan\psi \dot{\gamma}_{gr} \tag{3b}$$

In these relations, $\dot{\gamma}_{gr}$ and $\dot{\varepsilon}_{gr}$ denote the granular flow strain rates tangential and normal to the fault plane, respectively, and $\tan\psi$ denotes the average grain-grain dilatation angle, which can be written as $\tan\psi = 2H(\phi_c - \phi)$, where H is a geometric constant of order 1 (Niemeijer & Spiers, 2007; Paterson, 1995). The microscopic coefficient of friction of grain-grain contacts is given by Chen and Spiers (2016) as $\tilde{\mu} = \tilde{\mu}^* + \tilde{a}\ln\left(\dot{\gamma}_{gr}/\dot{\gamma}^*_{gr}\right)$, $\tilde{\mu}^*$ being a reference value of $\tilde{\mu}$ evaluated at $\dot{\gamma}^*_{gr}$ and $\tilde{a}$ being the coefficient of logarithmic rate-dependence of $\tilde{\mu}$.

We point out that Equation 3a simplifies to $\tau = \sigma\left[\tilde{\mu}^* + \tilde{a}\ln\left(\dot{\gamma}_{gr}/\dot{\gamma}^*_{gr}\right)\right]$ for $\phi \rightarrow \phi_c$ (and consequently $\tan\psi \rightarrow 0$). This simplified relation is directly comparable with the first two terms in the conventional rate-and-state friction formulation (Dieterich, 1979; Ruina, 1983):

$$\tau = \sigma\left[\mu^* + a\ln\left(\frac{V}{V^*}\right) + b\ln\left(\frac{V^*\theta}{D_c}\right)\right] \tag{4}$$

Here, μ^* is a reference friction coefficient corresponding with a slip rate V^*, θ encodes the "state" of the fault, and a, b, and D_c are constant coefficients. As such, granular flow is inherently a velocity-neutral or velocity-strengthening deformation mechanism. However, when acting in concert with a time-dependent strengthening mechanism (such as compaction by pressure solution creep), granular flow causes slip-dependent dilatation that counteracts the strengthening resulting from time-dependent compaction.

Hence, the interplay between dilatant granular flow and one or more compaction mechanisms gives rise to velocity-weakening behavior, depending on the relative rates of dilatation and compaction (see van den Ende & Niemeijer, 2018).

With the above constitutive relations for the relevant deformation mechanisms, the evolution of the macroscopic shear stress and gouge porosity of a zero-dimensional (spring-block) fault can be expressed in the following set of differential equations (Chen & Spiers, 2016):

$$\frac{\mathrm{d}\tau}{\mathrm{d}t} = k\left(V_{imp} - h\left[\dot{\gamma}_{gr} + \dot{\gamma}_{ps}\right]\right) \tag{5a}$$

$$\frac{\mathrm{d}\phi}{\mathrm{d}t} = -(1-\phi)\left(\dot{\varepsilon}_{gr} + \dot{\varepsilon}_{ps}\right) \tag{5b}$$

in which k is the effective shear stiffness (unit: Pa m^{-1}) of the fault. The instantaneous fault slip velocity V is obtained from the addition of the strain rates of granular flow and pressure solution (i.e., $V{=}h\left[\dot{\gamma}_{gr} + \dot{\gamma}_{ps}\right]$). In the QDYN seismic cycle simulator (Luo et al., 2017; van den Ende, Chen, et al. 2018), this set of ordinary differential equations is solved to compute the evolution of stress and porosity over the model fault (see Appendix A). In the present study, the localized zone thickness h is taken to be a constant, whereas it is expected to evolve over the course of a seismic cycle (e.g., due to the feedback between frictional heat production and fault weakening; Platt et al., 2014, 2015). Since we currently have no formulations available that describe the evolution of h and that are suitable for implementation in our numerical framework, we keep h constant throughout the simulations.

One important characteristic to note is that the steady-state velocity dependence of friction, that is, a material being velocity-strengthening or velocity-weakening, changes with velocity (see Figure 1c). As a result, classical rate-and-state friction is only comparable to the CNS model for small velocity perturbations around steady-state for which the velocity dependence $(a-b)$ can be approximated to be constant, so that the steady-state friction is proportional to $\log(V)$ (Chen & Niemeijer, 2017). With increasing departure from steady-state, both model frameworks predict different frictional behavior, as is notably seen in seismic cycle simulations (van den Ende, Chen, et al., 2018).

Finally, the adopted rheological model currently does not feature any high-velocity dynamic weakening mechanisms (see, e.g., Tullis, 2007). In the absence of dynamic weakening, the coseismic stress drop and maximum slip velocity as produced by the simulations are likely of smaller magnitude than anticipated for earthquakes in nature, where such mechanisms are known to operate. Accordingly, afterslip and interseismic creep likely constitute a larger portion of the total slip budget in the simulations than in nature. However, the earthquake nucleation process is likely unaffected by residual stress concentrations left by the previous seismic event, as the rheological contrasts between various fault segments generate a highly heterogeneous and dynamically evolving stress state over the fault, including many transient stress concentrations. Since this study considers the effect of rheological transitions on the nucleation of seismic events (during which dynamic weakening is inactive), we leave such an extension of the currently adopted model rheology for future studies.

2.3. Model Setup and Numerical Procedure

By employing a microphysical model that contains microstructural information, one can closely relate the model fault geometry to field and laboratory observations. In this work, guided by numerous field reports, we define heterogeneity through spatial variations in pressure solution kinetics, which reflect contrasts in fault rock composition or spatial variations in strain rate (see section 2.1). The model is motivated by the field observations of Fagereng (2011b) but may be extended to other cases or other scales. Following Fagereng (2011a), we assume that competent lenses (the asperities) obey a power law distribution in size, that is:

$$N(x) \propto x^{-D} \tag{6}$$

where $N(x)$ is the number of asperities of size x or greater and D is the fractal dimension (or power-law exponent). In outcrops of exhumed seismogenic subduction thrusts, D has been measured to fall in the range of $1.2 < D < 2.4$ (Fagereng, 2011a). Our procedure adopted to generate an asperity size distribution

Table 1
List of Symbols and Simulation Parameters and Their Respective Values or Ranges

Symbol	Description	Value	Units
$\tilde{a}$	Coefficient for logarithmic rate-dependence of $\tilde{\mu}$	0.006	—
c_s	Shear wave speed	3,000	m s^{-1}
D	Fractal dimension of size distribution	1–2	—
$\dot{\varepsilon}_{gr}$	Granular flow strain rate	var.	s^{-1}
$\dot{\varepsilon}_{ps}$	Pressure solution strain rate	var.	s-1
f	Asperity occupation ratio	0.4–0.6	—
ϕ	Gouge porosity	var.	—
ϕ_0	Lower cutoff porosity	0.03	—
ϕ_c	Critical state porosity	0.30	—
G	Shear modulus	30	GPa
$\dot{\gamma}_{gr}$	Granular flow shear strain rate	var.	s-1
$\dot{\gamma}^*_{gr}$	Reference $\dot{\gamma}_{gr}$ corresponding with $\tilde{\mu}^*$	$3 \times 10-9$	s^{-1}
$\dot{\gamma}_{ps}$	Pressure solution shear strain rate	var.	s^{-1}
h	Thickness of the gouge layer	10^{-2}	m
H	Dilatancy geometric constant	0.4	—
η	Radiation damping coefficient	0.5×10^6	Pa s m^{-1}
L	Length of periodic fault	16	km
$\tilde{\mu}$	Grain boundary friction coefficient	var.	—
$\tilde{\mu}^*$	Reference grain boundary friction coefficient	0.4	—
N	Number of fault elements	8,192	—
V	Fault slip velocity	var.	m s-1
V_{imp}	Imposed driving velocity	10^{-9}	m s-1
W/L	Amplitude-wavelength ratio of periodic faults	10	—
σ	Effective normal stress	50	MPa
τ	Shear stress	var.	Pa
tanψ	Dilatancy angle	var.	—
x_{max}	Maximum size distribution width	16	km
x_{min}	Minimum size distribution width	3.91	m
Z_{ps} (gouge)	Pressure solution kinetic parameter	$5 \times 10-16$	Pa^{-1} s^{-1}
Z_{ps} (matrix)	Pressure solution kinetic parameter	$3 \times 10-15$	Pa^{-1} s^{-1}

Note. "var." indicates that the quantity is a variable in the simulations.

that obeys the above relation is described in Appendix B. Following this procedure, we obtain a fault structure that is consistent with our interpretation of the field observations summarized in section 2.1. This fault geometry is projected onto a one-dimensional periodic fault, which represents an along-strike slice across a subduction thrust with along-strike segmentation (see Figure 1a; note that the "Field scale" and "Idealization" panels display an anti-plane view). The fault is subjected to an anti-plane imposed plate velocity $V_{imp} = 10^{-9}$ m s^{-1} and a uniform effective normal stress of $\sigma = 50$ MPa. The total extent of the fault ($L = 16$ km) is discretized evenly into $N =$ 8,192 fault elements, each of size $\Delta x = 1.95$ m. This mesh resolution is sufficiently small to resolve the rupture process zone, which has an estimated width of 21.45 m for the chosen set of parameters (see van den Ende, Chen, et al., 2018, their Appendix A).

It has been observed that pressure solution kinetics are accelerated in the presence of phyllosilicates (e.g., Hickman & Evans, 1995). The enhanced pressure solution rates in phyllonites can thus reasonably be argued to be due to the large abundance of phyllosilicates in the matrix that are thought to accelerate diffusive mass transfer rates (Bjorkum, 1996; Hickman & Evans, 1995; Renard et al., 2001). This reasoning holds for diffusion-controlled pressure solution creep, or in the case that the kinetics of diffusion and dissolution are of similar magnitude (Bernabé & Evans, 2007; Lehner & Leroy, 2004). Moreover, the chemistry of the pore fluid is known to exert strong controls on the rate of quartz dissolution, either enhancing (Dove, 1999; Rimstidt, 2015) or retarding (Iler, 1973) interface reaction rates depending on the presence of ionic species in the pore fluid. It is unclear which mechanism limits the rate of pressure solution under in situ thermodynamic and chemical conditions. However, field observations suggest that pressure solution rates are faster in the matrix than in the gouge, so for the kinetics of pressure solution Z_{ps}, we adopt values of 5×10^{-16} and 3×10^{-15} Pa^{-1} s^{-1} for the gouge and matrix, respectively. A value of $Z_{ps} = 3 \times 10^{-15}$ Pa^{-1} s^{-1} corresponds to theoretical estimates of Z_{ps} for mono-mineralic quartz at 250° and a grain size of 5 μm (Niemeijer et al., 2002). Other rheological and model parameters are summarized in Table 1.

The simulation is then run for at least 2,000 years, a time span over which all possible fault slip behavior is expected to be displayed. Owing to the finite simulated fault length ($L = 16$ km), the model outcomes will unavoidably be affected by the realization of the asperity distribution in the form of clustering and repeating events controlled by the local density of asperities. Therefore, the heterogeneous fault simulations are repeated with identical model parameters, but with a different random asperity distribution that has similar statistical properties as the first simulation set. We will refer to these two sets as Set 1 and Set 2 and consider the differences between them as stochastic variability. For the purposes of this study, we do not perform a detailed statistical analysis of the model results, as we only consider general trends as a basis for our interpretations and hypotheses.

3. Results

3.1. Seismic Character

As anticipated, the simulations with randomly heterogeneous faults show complex slip behavior controlled by the spatial and size distributions of asperities that litter the fault. This behavior is visualized in Figure 2 for simulation Set 1 by filled contour maps of the slip velocity as a function of the along-strike position and

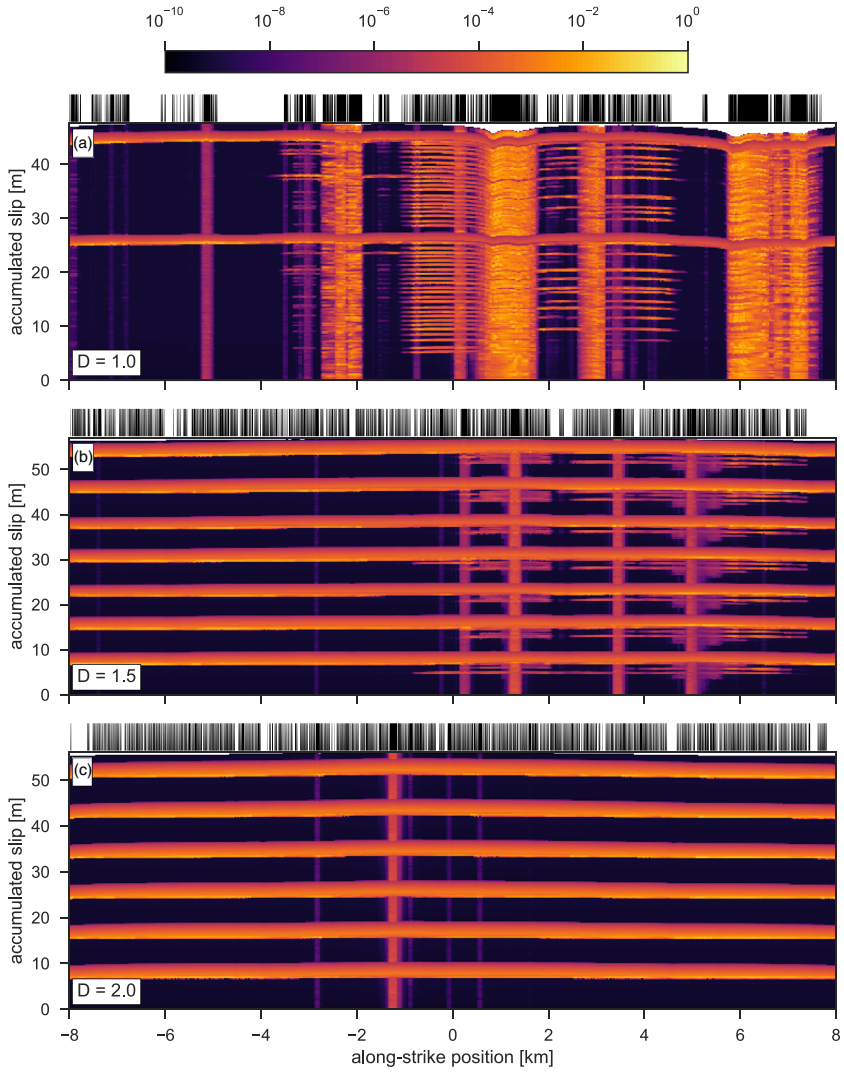

Figure 2. Filled contour maps of fault slip velocity (in $\mathrm{m\,s^{-1}}$) for simulation Set 1, with $f = 0.5$. (a) $D = 1$ (same as Figure 3b): Numerous P-instabilities of various magnitudes cluster around fault localities of high asperity density, and T-instabilities occur infrequently; (b) $D = 1.5$: Quasi-periodic T-instabilities are interspersed with small P-instabilities; (c) $D = 2$: P-instabilities exist only as small slow slip events. T-instabilities occur periodically with no precursory activity; For each simulation, the spatial distribution of asperities is plotted as a "barcode" above each panel, with each black bar representing an asperity.

accumulated slip, for three simulations characterized by asperity distribution exponents (D) of 1, 1.5, and 2, all exhibiting an asperity occupation ratio of $f = 0.5$. For reference, the asperity distribution of each simulation is indicated by the "barcode" above each panel in Figure 2, in which the black bars represent the asperities. In the simulation with $D = 1$ (Figure 2a), unstable slip is predominantly produced in the form of small (a)seismic events that cluster around areas of high asperity density on the fault. Areas of low asperity density mostly creep at a steady rate. Fault regions of high asperity density rupture predominantly seismically, in which clusters of asperities fail simultaneously. We define these seismic events that rupture only a portion of the fault as partial instabilities, or P-instabilities for short. This definition of a P-instability deviates from that proposed by Luo and Ampuero (2018), who reserved this term for the failure of individual asperities, thereby excluding simultaneous rupture of small clusters of asperities. Since the focus of this work is directed at fault-spanning events, we classify any type of partial fault rupture as a P-instability. Conversely, we classify complete fault rupture as a total instability, or T-instability. Within the simulated time of 2,000 years, two fault-spanning T-instabilities are produced in

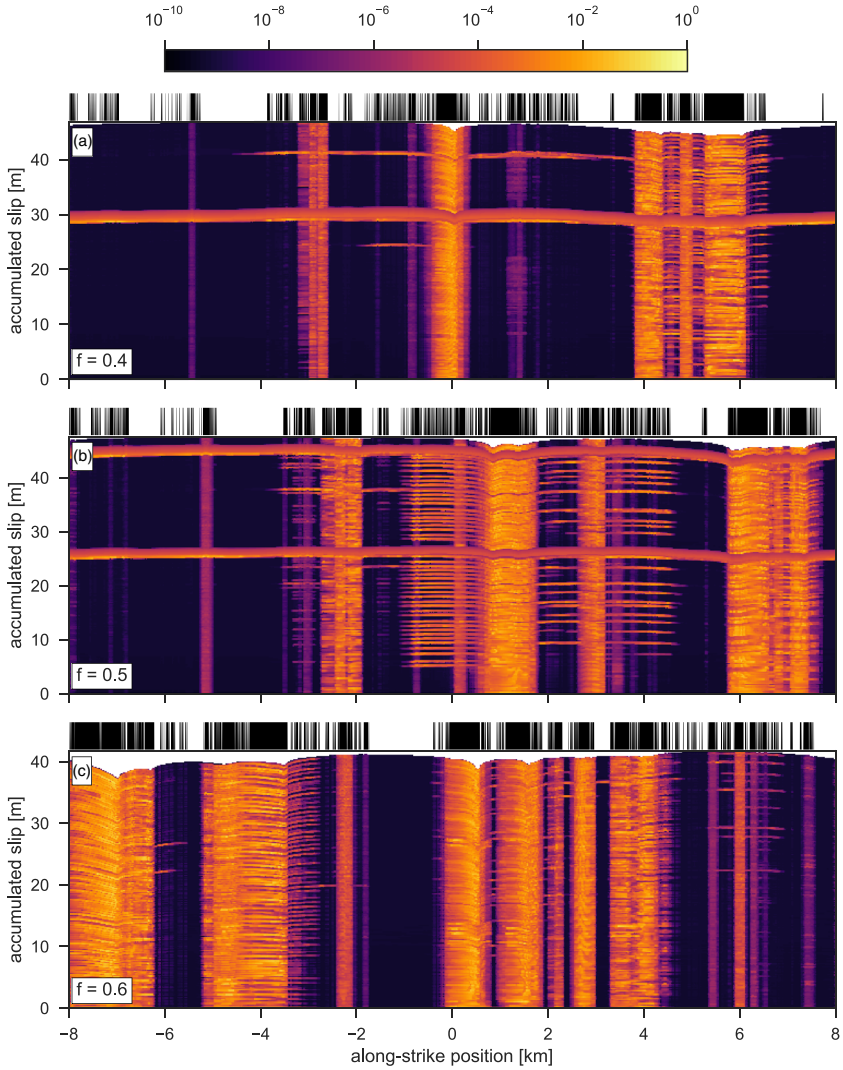

Figure 3. Filled contour maps of fault slip velocity (in m s^{-1}) for simulation Set 1, with $D = 1$. (a) $f = 0.4$: P-instabilities are sparsely covered over the model fault, with occasional P-events that extend over a larger area; (b) $f = 0.5$ (same as Figure 2a): Several P-events extend outside of their characteristic source region; (c) $f = 0.6$: P-instabilities are predominantly confined to their characteristic source regions; for each simulation, the spatial distribution of asperities is plotted as a "barcode" above each panel, with each black bar representing an asperity.

the simulation with $D = 1$ (Figure 2a). No clearly interpretable precursory activity is seen that forecasts an imminent T-instability, and following a T-instability, there appears to be a brief period of seismic quiescence near the center of the fault.

In contrast to the simulation with $D = 1$, the simulation with $D = 1.5$ (Figure 2b) exhibits frequent, quasi-periodic T-instabilities that constitute about half of the total fault slip budget. Each T-instability is preceded by P-instabilities that increase in extent in the advent of a T-instability. These P-instabilities also cluster near regions of higher asperity density, although the spatial asperity distribution is more diffuse than in the simulation with $D = 1$. Remarkably, in the simulation with $D = 2$ (Figure 2c), there exist only two modes of unstable slip: The P-instabilities are periodic slow slip events that are each confined to a single asperity cluster just large enough to nucleate a frictional instability, and the T-instabilities occur periodically (approximately every 300 years) with no precursory activity.

The effect of varying f is illustrated in Figure 3 in a similar way as in Figure 2, with $D = 1$ and $f = 0.4$, 0.5, and 0.6. The seismic character of each of these simulations is very similar, with numerous P-events occurring in fault regions of high asperity density, and the occasional occurrence of a T-instability in $f = 0.4$ and 0.5. The

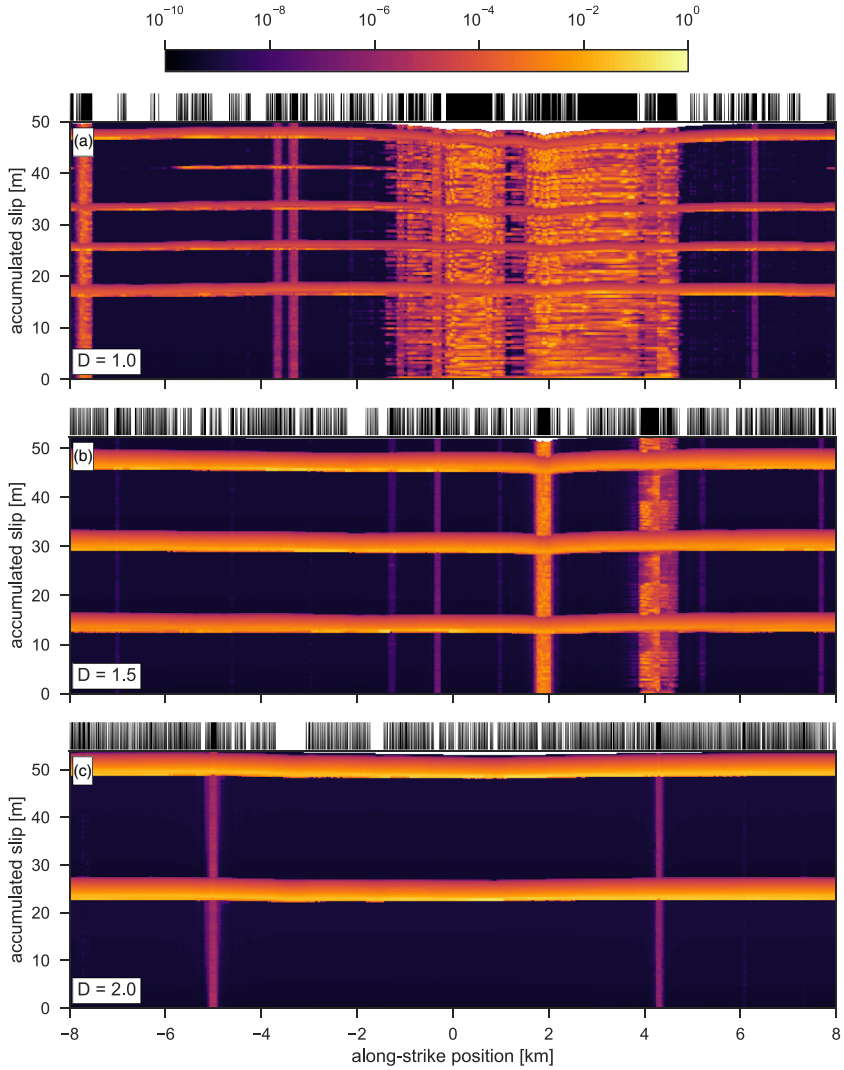

Figure 4. Filled contour maps of fault slip velocity (in $\mathrm{m\,s^{-1}}$) for simulation Set 2, with $f = 0.5$. (a) $D = 1$ (same as Figure 5b): Numerous P-instabilities of various magnitudes cluster around fault localities of high asperity density, and T-instabilities occur infrequently; (b) $D = 1.5$: Quasi-periodic T-instabilities are interspersed with small P-instabilities; (c) $D = 2$: P-instabilities exist only as small slow slip events. T-instabilities occur periodically with no precursory activity; for each simulation, the spatial distribution of asperities is plotted as a "barcode" above each panel, with each black bar representing an asperity.

simulation with $f = 0.6$ does not display any T-instabilities, which will be discussed further in section 4.1. For larger values of f, larger portions of the fault exhibit P-instabilities.

The results of simulation Set 2 are presented in Figures 4 and 5. While the behavior seen in simulation Set 2 is broadly similar to Set 1, there are a few notable differences between the two, most likely caused by variations in local asperity density. Overall, the recurrence time of the T-instabilities in Set 2 with $D > 1$ is significantly longer than seen in Set 1, and accordingly, the total displacement in one such T-instability is much larger. Also, no precursory events are seen in Set 2 with $D = 1.5$, which instead shows repeating small earthquakes. In the simulations with $D = 1$, the recurrence time of T-events is shorter in Set 2, although there is some aperiodicity to each cycle. Simulation Set 2 with $f = 0.6$ exhibits one (but small) T-instability, as opposed to its equivalent in Set 1.

A quantitative way of comparing the various heterogeneous fault simulations is by considering the (normalized) frequency-magnitude relations—see Figure 6. In this figure, the effect of individual asperities and asperity clusters manifests itself as steep drops in frequency with increasing M_w, as a result of numerous

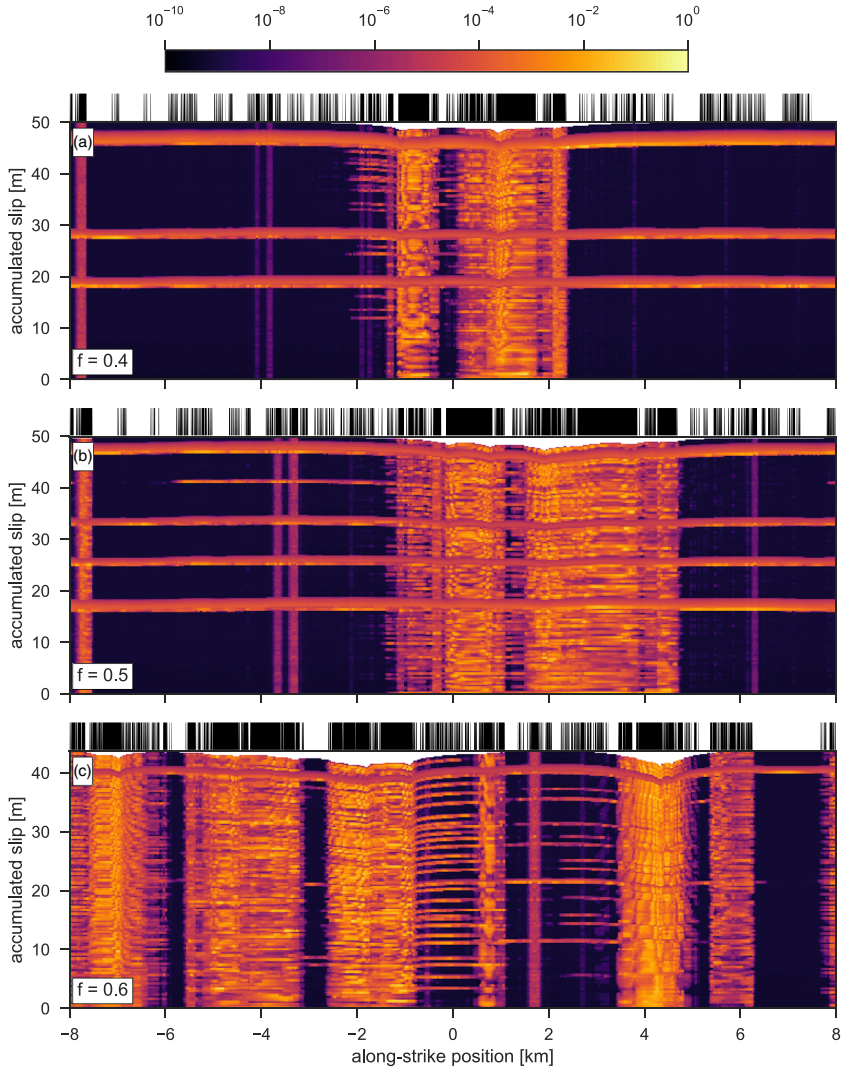

Figure 5. Filled contour maps of fault slip velocity (in m s^{-1}) for simulation Set 2, with $D = 1$. (a) $f = 0.4$: P-instabilities are sparsely covered over the model fault, with occasional P-events that extend over a larger area; (b) $f = 0.5$ (same as Figure 4a): Several P-events extend outside of their characteristic source region; (c) $f = 0.6$: P-instabilities are predominantly confined to their characteristic source regions; for each simulation, the spatial distribution of asperities is plotted as a "barcode" above each panel, with each black bar representing an asperity.

repeating events on the same section of the fault (same M_w). This is particularly apparent for larger event magnitudes, as events nucleating in one given site fail to link up with other seismogenic sites, resulting in a corner magnitude related to the largest seismogenic cluster of asperities. However, all simulations, with the exception of $f = 0.6$ in Set 1, show T-instability events that span the entire fault. For some simulations, such as $f = 0.5$ and $D = 1$, it could be argued that these T-events follow the frequency-magnitude relation defined by regular events and that T-events simply extend the existing range of P-events. On the other hand, this argument does certainly not hold for simulations with $D > 1$, particularly when it is considered that these simulations contain a large number of (small) slow slip events that would likely not be registered by surface monitoring stations, so that a real-world equivalent frequency-magnitude distribution would appear differently (or be absent).

3.2. Fault Stress and Slip Deficit

The local state of stress is of crucial importance in determining both the slip velocity and stability of a particular fault segment. To gain some insights into the evolution of fault stress, we calculate the coefficient of

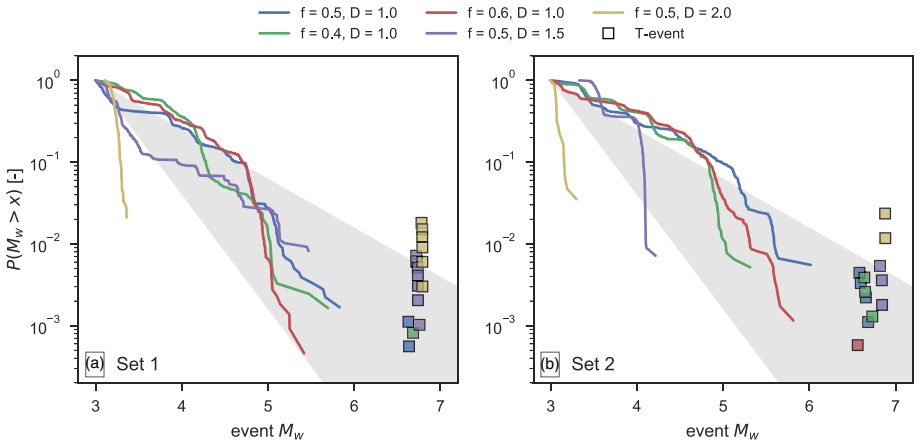

Figure 6. Frequency-magnitude distributions of the heterogeneous fault simulations for events of $M_w > 3$ (including slow slip events). T-instabilities are marked as individual squares. Gray shaded areas indicate the range of Gutenberg-Richter *b*-values (0.6<*b*<1.4) observed by Marzocchi et al. (2016). (a) Frequency-magnitude distributions for the simulations in Set 1; (b) frequency-magnitude distributions for the simulations in Set 2.

friction (τ/σ) at which the fault operates, averaged over the asperities, the matrix, and the total fault length (Figure 7). By doing so, we observe the following:

1. For simulations characterized by $D = 1$, the average stress supported by the asperities varies around a time-constant value; that is, the long-term asperity stress is constant, with small stress drops due to P-events. With each P-event, the average stress supported by the matrix is perturbed. This perturbation decays with time while the asperities are reloaded.
2. In the simulations with $D = 1$ and $f = 0.4$ and 0.5, long-term loading of the matrix by P-events and tectonic motion leads to a net increase in fault stress, until a critical stress level is achieved and a T-instability is generated.
3. In the simulation with $D = 1$ and $f = 0.6$, the fault stress levels off to a time-constant value, after which all deformation is accommodated by P-events and creep of the matrix. In simulation Set 1, no T-instability is generated within the simulated time span of 2,000 years, nor are there indications that it will occur in the future. In simulation Set 2, one T-instability is generated, but it is relatively small in magnitude. The average stress level that is reached in these simulations is close to the critical value of other simulations with $D = 1$.

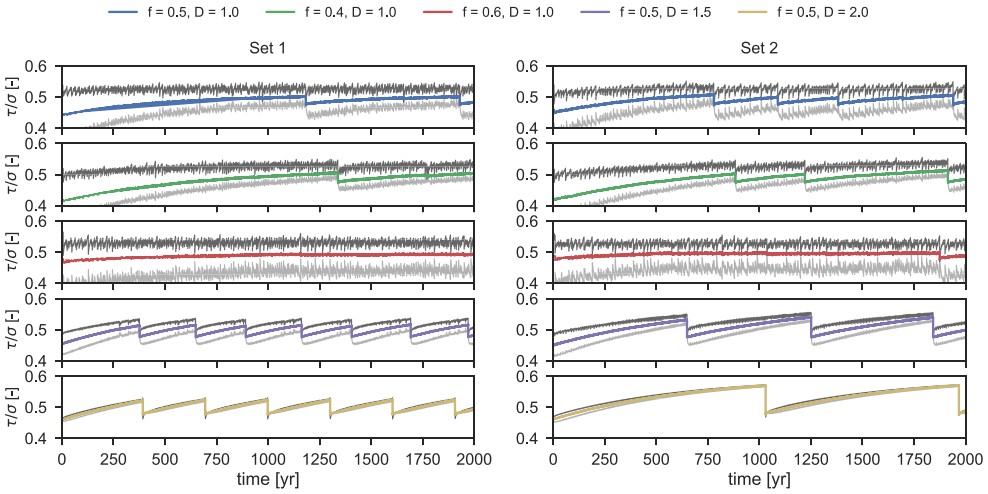

Figure 7. Average coefficient of friction (τ/σ) under which the model fault operates, for all heterogeneous fault simulations (parameters as indicated in the legend). The average friction supported by the asperities and matrix is indicated by the dark and light gray curves, respectively.

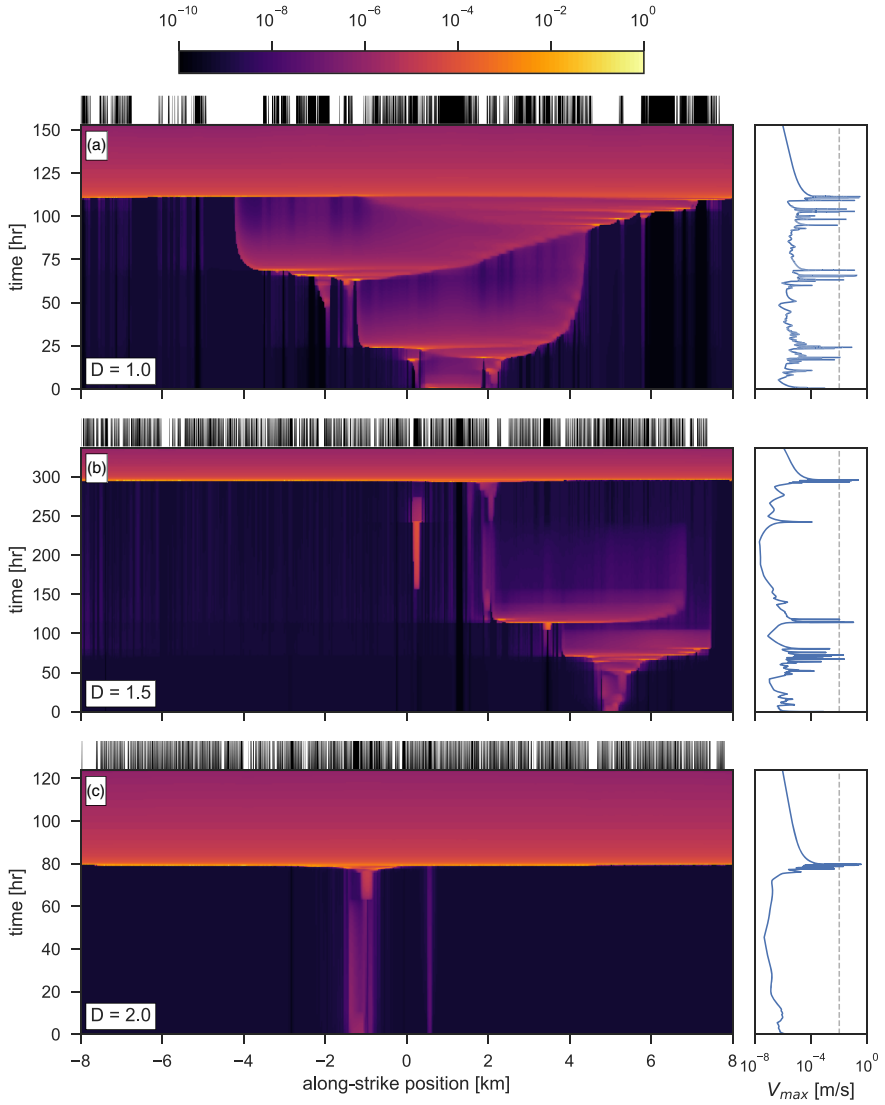

Figure 8. Filled contour maps of fault slip velocity (in m s^{-1}) immediately prior to nucleation of the last T-instability, for each simulation in Set 1 with $f = 0.5$. (a) $D = 1.0$: P-instabilities dynamically cascade up over a duration of about 4 days prior to the T-event, producing a sequence of foreshocks; (b) $D = 1.5$: P-instabilities fail to cascade up, but afterslip facilitates the nucleation of a T-instability. Note that the nucleus for the T-instability is small; (c) $D = 2.0$: The T-event emerges from a small nucleus that rapidly grows into an instability.

4. In the simulations with $D > 1$, the average stress on the asperities is not constant in time and follows a similar stress evolution as the matrix. In simulation Set 1 with $D = 1.5$, P-instabilities of increasing magnitude emerge when stresses are sufficiently large. In both cases, periodic T-instabilities are generated when a critical value of stress is reached similar in value to the simulations with $D = 1$. However, the recurrence times observed in both simulation sets are markedly different, ranging from about 250 years in Set 1, to close to 1,000 years in Set 2.
5. Although the simulations with $D = 2$ accommodate slip predominantly through stable creep, the long-term buildup of stress indicates that the fault-averaged creep rates are lower than the imposed loading velocity.

3.3. Nucleation and Initiation of T-Instabilities

Let us now consider the nucleation stage of T-instabilities for various values of D (Figures 8 and 9; note that the vertical axis scale varies between panels). In the simulations with $D = 1$, consecutive P-instabilities cascade up (i.e., their rupture areas link up) over a period of about 4 days prior to the T-event, ultimately

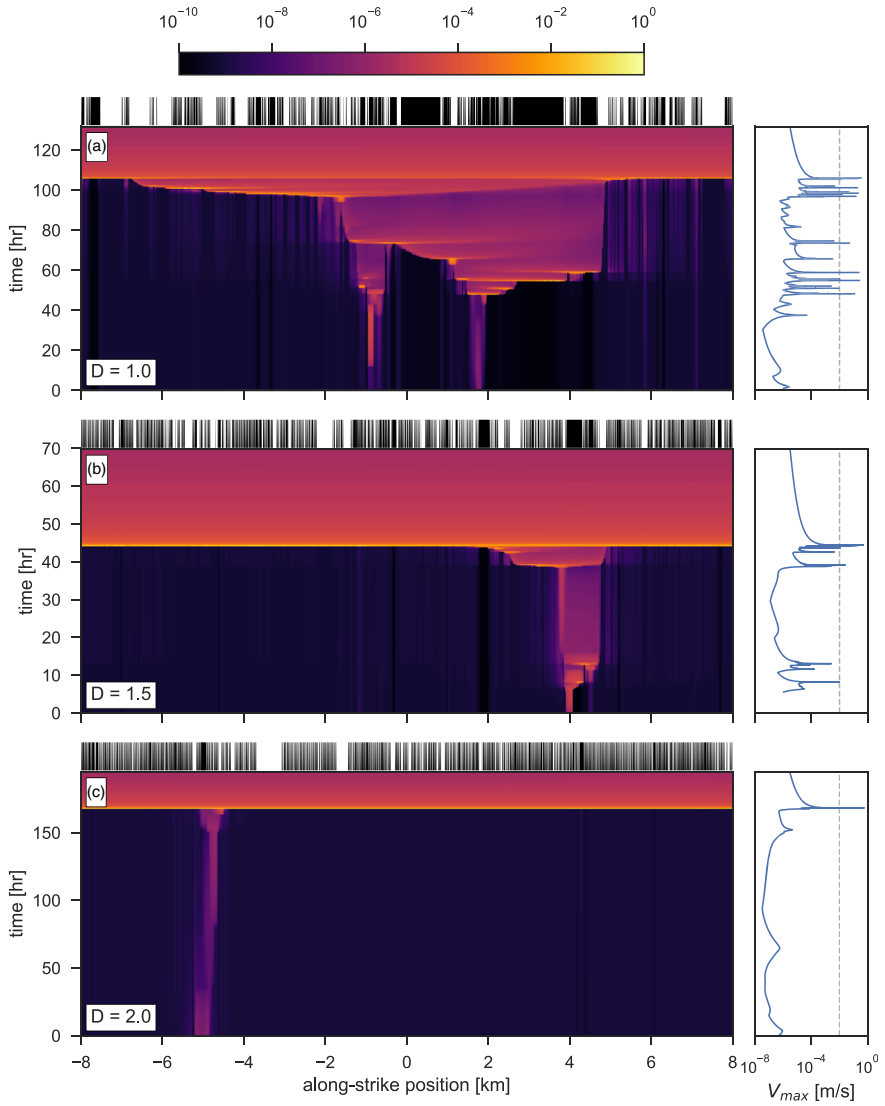

Figure 9. Filled contour maps of fault slip velocity (in m s^{-1}) immediately prior to nucleation of the last T-instability, for each simulation in Set 2 with $f = 0.5$. (a) $D = 1.0$: P-instabilities dynamically cascade up over a duration of about 2 days prior to the T-event; (b) $D = 1.5$: P-instabilities cascade up into a T-instability, but the extent of the final nucleation region is much smaller than observed in simulations with $D = 1$; (c) $D = 2.0$: The T-event emerges from a small nucleus that rapidly grows into an instability.

triggering a T-instability borne out of a large nucleus (spanning more than half of the periodic width of the fault). The hypocentres of the P-events migrate along the perimeter of the nucleus as a sequence of foreshocks, and the T-event itself shows a heterogeneous spatial distribution of slip velocity.

The simulation with $D = 1.5$ in Set 1 displays a failed cascade-up sequence, with a temporal gap of about 1 week between the last seismogenic P-instability and the T-event. However, the nucleation region of the T-instability appears to grow out of afterslip following the last P-event, hinting that nucleation of the T-instability is facilitated by afterslip. In simulation Set 2, P-events manage to cascade up over a time span of less than 2 days, though the nucleus for the T-instability is significantly smaller than observed in the simulations with $D = 1.0$. In contrast with the above, the simulations with $D = 2$ show no signs of cascading P-events. The T-instabilities nucleate seemingly spontaneously and abruptly from a minute nucleation patch, extending only a fraction of the total periodic fault width. In addition, the T-event is rather homogeneous in its spatial distribution of slip velocity.

The question whether nucleation of a T-instability occurs within a matrix segment or an asperity segment is somewhat ambiguous, as the vast majority of the segments are smaller than the (lower bound) nucleation length of 23.2 m calculated for a homogeneous fault composed of only asperity materials (see Appendix C). Substituting $x = 23.2$ m in Equation B2b, we find that for $D = \{1,1.5,2\}$, the fraction of asperities larger than this nucleation length is 0.17, 0.07, and 0.03, respectively. Hence, the nucleation process of T-instabilities most certainly involves multiple segments. Instead, one could view the nucleation process in the context of the overall seismic character of the fault, that is, whether a fault is seismically active or predominantly creeping. Taken in this context, nucleation can be said to occur on a creeping fault, even though this does not necessarily imply that only matrix segments were involved in the nucleation process or that matrix segments can self-nucleate instabilities without external perturbations (e.g., from neighboring asperities).

4. Discussion

4.1. Mechanisms Behind T-Instabilities and Generality of Results

In the CNS model formulation adopted in this study, strain is accommodated through the parallel operation of nondilatant pressure solution creep and dilatant granular flow, for which the constitutive relations are given by Equations 1 and 3, respectively. For the purpose of this discussion, we can consider the shear strength of the fault to follow one of two end-member cases, one in which pressure solution creep dominates over granular flow (i.e., $\dot{\gamma}_{ps} \gg \dot{\gamma}_{gr}$) and one where the converse is true ($\dot{\gamma}_{ps} \ll \dot{\gamma}_{gr}$). For each of these two end-member scenarios, the shear strength as a function of the imposed shear strain rate ($\dot{\gamma} = V_{imp}/h$) follows directly from the above-mentioned constitutive relations:

$$\tau_{ps} = \frac{\dot{\gamma}}{Z_{ps} f_1(\phi)} \tag{7a}$$

$$\tau_{gr} = \frac{\widetilde{\mu} + \tan\psi}{1 - \widetilde{\mu}\tan\psi}\sigma \tag{7b}$$

where τ_{ps} and τ_{gr} denote the end-member shear strengths of pressure solution and granular flow, respectively. Recall that $\widetilde{\mu} = \widetilde{\mu}^* + \tilde{a}\ln\left(\dot{\gamma}/\dot{\gamma}^*_{gr}\right)$ and $\tan\psi = 2H(\phi_c - \phi)$, which makes τ_{gr} an explicit function of strain rate and porosity.

In the two-mechanism model (at steady-state), the boundary between the ductile creep regime and the cataclastic granular flow regime is marked by the intersection of the two end-member strength curves (i.e., $\tau_{ps} = \tau_{gr}$). Consider now a fault segment that underwent deformation in the creep regime for sufficiently long durations so that $\phi \to \phi_0$ (and $\tau = \tau_{ps} < \tau_{gr}$), marked by point 1 in Figure 10. Next, the imposed tectonic loading or a perturbation in shear stress will drive point 1 towards higher strain rates and closer to the transition to granular flow, as indicated by point 2. In the case that no further stressing occurs, the initial perturbation will decay by ductile creep, and so the system returns to point 1. However, for incremental slip of the asperity in the form of P-events, or for continuous loading (due to tectonic motion), the incremental or continuous buildup in stress will drive the system towards a critical point that marks the onset of granular flow (point 3). By its own nature, operation of granular flow induces dilatation, and so at the critical point, the gouge porosity starts to increase ($\phi > \phi_0$). Following Equation 7b, an increase in porosity (i.e., a decrease in $\tan\psi$) causes substantial lowering of τ_{gr}, and so, the fault rapidly weakens with increasing shear strain as ϕ increases in accordance with Equations 3b and 5b (point 4 and inset). Hence, for a sufficiently low self-stiffness, a frictional instability is generated, and the fault accelerates. After the slip event, the fault returns to its initial state (point 1), and the same process may reoccur. A similar conceptual interpretation for the nucleation of instabilities was recently proposed by Verberne et al. (2017), on the basis of laboratory observations. We note that, as can be seen from Equation 7b, the granular flow strength is only weakly dependent on strain rate. Hence, the quantity that governs earthquake nucleation in our models is the instantaneous shear stress and not the strain rate or stressing rate. Furthermore, at the transition from velocity-strengthening ductile creep to velocity-weakening granular flow, it is expected that deformation

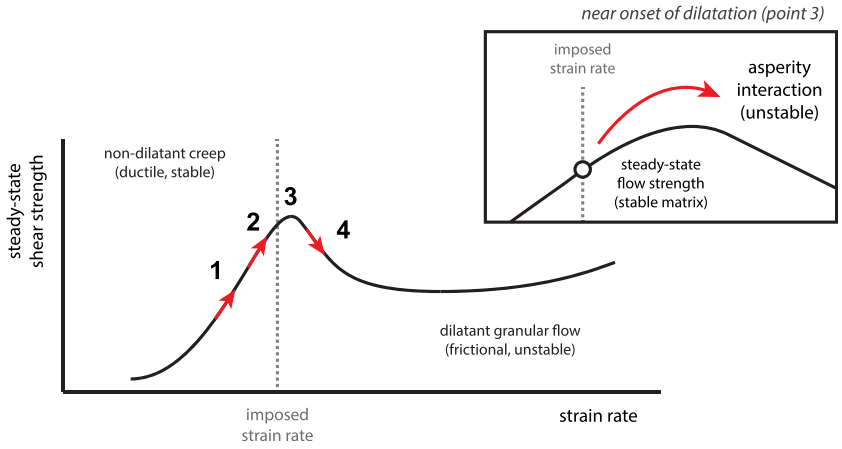

Figure 10. Schematic diagram of the steady-state strength profile of the matrix, as a function of strain rate. The generation of a T-instability is characterized by a transition from nondilatant ductile creep (stable) to dilatant granular flow (unstable). At a given moment in time, the stress supported by the matrix is indicated by point 1. Due to tectonic loading and nonuniform fault slip, the stress on the matrix increases (point 2). At a critical value of stress, the matrix enters the dilatant granular flow regime, and a T-instability nucleates.

becomes increasingly more localized (Beeler et al., 1996), causing additional divergence away from the point of velocity-neutrality once nucleation has commenced.

With the detailed description of the nucleation mechanism of frictional instabilities, we can continue to interpret the spectrum of slip behavior displayed in the simulations. When inspecting the stresses acting across the model faults (Figure 7), we observe that the average stress supported by the matrix increases over time until a critical stress is achieved that triggers the nucleation of an instability in fault segments that were previously creeping stably in the ductile regime (going from point 1 to point 3 in Figure 10). When large parts of the fault are near-critically stressed, the stress perturbation caused by an approaching rupture front facilitates cascade-style failure of the fault in its entirety (point 3 to point 4 in Figure 10). The occurrence of such a T-instability on a heterogeneous fault could be analogous to great earthquakes in nature, such as megathrust ruptures. We will explore this idea further in section 4.3.

Two peculiar model outcomes that are still left unexplained are the absence of T-instabilities in the simulation with $f = 0.6$ and $D = 1$ (exhibiting abundant P-events; see Figure 3c) and the occurrence of T-instabilities in simulation Set 1 with $D = 2$ (exhibiting only minute slow slip events; see Figure 2c). In the first case ($f = 0.6$), it can be seen in Figure 7 that the average fault stress no longer increases after about 1,000 years, which indicates that the long-term fault slip rates equal the tectonically imposed velocities, so that no elastic strain accumulates. In other words, the combination of stable creep of the matrix and seismic moment released by the P-events balances the slip budget. The ductile creep rate of the matrix at this steady-state level of stress, in combination with unstable slip of the asperities, is sufficient to accommodate the imposed strain rate, and so, no T-instabilities are required to balance the slip budget.

Conversely, the simulations with $D = 1.5$, and in particular $D = 2$, show continuous buildup of elastic stress with little or no moment release by P-events. Note that, even though these simulations show stable creep on time scales shorter than about 250 years, still 50% of the fault plane consists of (velocity-weakening) asperities that exhibit lower pressure solutions rates than the phyllonite matrix and so deform at strain rates that are lower than what is imposed. For the chosen value of Z_{ps} of the matrix, and in the situation that no asperities would be present (i.e., $f = 0$), the fault would accommodate the imposed strain entirely by ductile creep and would therefore be perfectly stable. Hence, the asperities effectively act as a "brake" in moderating fault creep rates to lower values (due to the "stress shadow" effect Bürgmann, 2005), and as a result, the stresses on the fault increase over time. One crucial aspect here is that the spatial and size distribution of the asperities is diffuse owing to its high fractal dimension, so that strain accommodation is distributed over the entire fault and no single asperity or cluster of asperities is large enough to generate large instabilities (fast earthquakes). This observation complements previous numerical studies (Dublanchet et al., 2013; Luo &

Ampuero, 2018; Skarbek et al., 2012; Yabe & Ide, 2017) that considered only variations in the value of f to control the seismic character of heterogeneous faults. Moreover, the model outcomes in this respect are in good agreement with the field observations of Fagereng (2011a), who concluded that deformation observed on an outcrop scale was localized for $D<1.4$, and distributed for $D > 1.4$, with mixed-mode deformation features observed at $D\approx1.4$. In the model simulations, we observe predominant seismic slip at $D = 1$, (short-term) stable creep at $D = 2$, and mixed-mode behavior at $D = 1.5$. However, the simulations with $D \geq 1.5$ still exhibit long-term T-instabilities, for which no direct evidence was observed by Fagereng (2011a).

In this study, the structure and rheology of the model fault were motivated mainly by the geological observations of Fagereng et al. (2011a, 2011b) on exhumed subduction thrust interfaces. However, the mechanism for generating T-instabilities described above does not specify the tectonic setting (e.g., subduction thrust versus continental fault). Hence, our numerical observations may be placed in a broader tectonic context, provided that (1) rheological transitions from rate-strengthening to rate-weakening are feasible within the range of in situ thermodynamic conditions and material properties and (2) spatial heterogeneity of the rheological properties within the fault zone is persistent, in the sense that rheological contrasts are not removed over the time scale of a seismic cycle. Moreover, we expect that the details of the processes underlying the transition from rate-strengthening to rate-weakening are not immediately relevant, but rather that any combination of processes leading to such transition is sufficient to generate frictional instabilities on creeping faults.

4.2. Comparison With Rate-and-State Friction

On the basis of the previous analysis, we can now compare the interpretation of T-instabilities predicted by the CNS model with previous analyses based on rate-and-state friction. The occurrence of T-instabilities in a periodic single-asperity system was investigated in great detail by Luo and Ampuero (2011a). Based on their observations, seven dimensionless parameters were identified to control the transition from P- to T-instabilities and the seismic character of the system. In this discussion, we will restrict ourselves to the relative strength α_R and area ratio f', which are defined as

$$\alpha_R \equiv \frac{(b_w - a_w)\sigma_w}{(a_s - b_s)\sigma_s} \tag{8a}$$

$$f' \equiv L_w/L_s \tag{8b}$$

In the above definitions, subscripts w and s denote the regions of velocity-weakening (VW) and velocity-strengthening (VS), respectively, a and b denote the rate-and-state friction constitutive parameters (see, e.g., Marone, 1998), and L_x is the length of a particular region (either VW or VS). In this study, $\sigma_w = \sigma_s = \sigma$. Recall that the area ratios f' (used by Luo & Ampuero, 2018) and f (used in this study) are related through $f' = f/(1-f)$. The relative strength parameter α_R represents the strength contrast between the velocity-weakening asperity and velocity-strengthening matrix. Depending on the chosen values of α_R and f', the fault would rupture either partly in a P-instability, or fully in a T-instability. Mixed-mode behavior, that is, simulations exhibiting both P- and T-instabilities, only emerged for large values of α_R (strong VW of the asperity compared to the degree of VS of the matrix). Mixed-mode behavior would manifest itself as P-instabilities preceding a T-instability in the form of foreshocks, or as supercycle behavior defined by clustered occurrences of fault-spanning ruptures interspersed by P-instabilities. By increasing f', the critical value of α_R at which T-instabilities and mixed-mode behavior emerge, decreases; that is, the system becomes more prone to a T-instability when the area of the asperity is large. It was found that the critical value of α_R that marks the transition decreases approximately as $1/f'$.

Since classical rate-and-state friction (as adopted by Luo & Ampuero, 2018) assumes constant values of a and b, there exists no transition from velocity-strengthening ($(a-b) > 0$) to velocity-weakening ($(a-b)<0$) with increasing slip velocity. Therefore, the occurrence of T-instabilities is purely of geometrical origin: If the size of the VS region is small (large f'), or if its resistance to accelerated slip is small (large α_R), a rupture nucleating in the VW asperity may traverse the VS region and link up with neighboring asperities. Note that the fault geometry adopted by Luo and Ampuero (2018) consists of a periodically repeating pair of one VW and one VS patch, so that the rupture emanating from the asperity links up with itself. This interpretation

is supported by previous numerical work (e.g., Tinti et al., 2005), detailed further by Skarbek et al. (2012), Dublanchet et al. (2013), Luo and Ampuero (2018), and others. However, in the CNS model, the equivalent values of $(a-b)$ in the ductile creep regime (i.e., $\mathrm{d}(\tau_{ps}/\sigma)/\mathrm{dln}V$) is of the order of τ_{ps}/σ, which is one or more orders of magnitude larger than the equivalent (steady-state) values of $(b-a)$ in the granular flow regime (see van den Ende, Chen, et al., 2018, for derivation and discussion). A value of $(a-b)$ of, for example, in the creep regime may seem excessive compared to values typically reported by laboratory studies and used in numerical models (in the range of $\pm 10^{-2}$; see Scholz, 2019). However, most of the laboratory studies reporting these values of $(a-b)$ do not achieve pressure and/or temperature conditions required for steady-state deformation in the ductile creep regime. In experiments that do achieve such conditions, "anomalous" values of $(a-b)$ are observed up to 0.2 (Blanpied et al., 1998; Shimamoto, 1986; Verberne et al., 2017). Furthermore, it has been argued that $(a-b)$ in this regime scales inversely proportional to the stress exponent n of the deformation mechanism, that is, $(a-b)=\tau/n\sigma$, so that deformation mechanisms other than pressure solution may exhibit lower values of $(a-b)$ (Chen & Niemeijer 2017; Shimamoto & Noda, 2014). Therefore, reasonable values of α_R predicted for the ductile creep regime are of order 0.1 or less, which would require $f'>10$ ($f>0.9$) to facilitate T-instabilities in CNS-governed model faults. The fact that fault-spanning ruptures are observed in simulations with f' in the range of 0.6–1.5 (f in the range of 0.4–0.6) indicates that the occurrence of the observed T-instabilities cannot be explained by geometry alone and that the rheology of the fault, namely, the transition from nondilatant to dilatant deformation, plays a crucial role.

In a two asperity system, Kaneko et al. (2010) investigated the probability that both asperities rupture in a single event, as a function of their separation distance and strength contrast between the VW asperities and surrounding VS matrix. Similar to Luo and Ampuero (2018), a dimensionless control parameter B was defined to indicate the barrier efficiency of the interstitial VS patch, which could be approximated as

$$B \approx \frac{20(a_s-b_s)\sigma}{\beta\Delta\tau_w}\,\frac{D_s}{D_w} \tag{9}$$

Here, D_s is the extent of the VS region separating the two asperities, each of length D_w, β is a geometric factor chosen as 1/2 in the 2-D simulations of Kaneko et al. (2010), and $\Delta\tau_w$ is the stress drop averaged over the VW asperity (typically of order 0.1σ). These authors showed that the probability of a two-segment rupture, that is, a rupture successfully traversing the VS segment, decreased proportional to B, reaching zero near $B\approx 1.5$. For $B>2$, no two-segment ruptures were observed over 9,000 years of simulated time, suggesting a hard threshold value of B above which the VS segment acts as a permanent barrier to dynamic rupture. When a value of $(a-b)=0.1$ is taken (a realistic value for the deformation regime expected for a phyllonite matrix), then a threshold value of $B=2$ would correspond to a ratio of $D_s/D_w=0.05$. This value translates roughly to $f'=40$ ($f=0.98$). Since a two-segment rupture in the geometry of Kaneko et al. (2010) can be interpreted as a T-instability in the framework of Luo and Ampuero (2018), we can conclude on the basis of microphysical and rheological considerations that multi-asperity ruptures occurring as proposed by Kaneko et al. (2010) and Luo and Ampuero (2018) exist only when asperities are separated by an insignificantly small patch of phyllonitic matrix (which is not observed in geological outcrops).

Similar to the work of Kaneko et al. (2010), the behavior of a two-asperity system was investigated numerically by Noda and Lapusta (2013), additionally considering the effects of high-velocity dynamic weakening (thermal pressurization). In the study of Noda and Lapusta (2013), one of the two patches (patch A) exhibited $(a-b)<0$, with a low dynamic weakening efficiency. The other patch (patch B) exhibited $(a-b)>0$ in the quasi-static (aseismic) regime, but with efficient dynamic weakening under coseismic slip velocities. A key result of this work is that the nominally stable patch B could still be triggered to undergo a dynamic instability for a sufficiently large perturbation induced by patch A. This behavior is analogous to the P- and T-instabilities observed in this study, with the T-instability being facilitated by a rheological transition. However, the slip velocity at which dynamic weakening becomes efficient lies in the range of coseismic slip velocities (Tullis, 2007), so that this mechanism is not viable at typical nucleation rates (10^{-9} to 10^{-6} m s^{-1}). On the other hand, the rheological transitions predicted by the CNS model are not mutually exclusive with those due to dynamic weakening. Since it is likely that one or more dynamic weakening mechanisms

operate in natural faults, it is conceivable that a fault segment experiences multiple rheological transitions going from nucleation slip rates to coseismic slip rates.

4.3. Interpreting T-Instabilities as Giant Earthquakes

It was argued in previous sections that the T-instabilities produced in the numerical simulations are analogous to great and giant earthquakes occurring in nature. Time-dependent loading of a creeping matrix, along with a transition from nondilatant to dilatant deformation, offers a mechanism by which a strongly velocity-strengthening fault segment may propagate or even nucleate dynamic rupture instabilities, facilitating multi-asperity ruptures. In this way, an entire fault segment (or multiple fault segments) may rupture in a single event as seen in great and giant earthquakes (e.g., Johnson et al., 1996; Lay et al., 2005). In a classical rate-and-state friction interpretation of multi-asperity rupture, T-instabilities may only occur for a highly restricted and unrealistic range of parameters, owing to the large values of $(a - b)$ of the ductile matrix, as resulting from the present model formulations (see section 4.2).

In the numerical simulations, the stress supported by the ductile matrix was observed to continuously increase through incremental loading by regular earthquakes or slow slip events, or through predominantly stable creep at rates lower than the imposed loading velocity. Overall, fault stress increased due to an increasing global slip deficit, which was relieved by T-instabilities. Closing of the slip budget as required for conservation of seismic moment has been proposed as the underlying reason for giant earthquakes in subduction zone settings (Kagan & Jackson, 2013; Satake & Fujii, 2014; Stevens & Avouac, 2016), although these studies do not specify the exact micromechanism. The stress-driven transition from ductile creep to granular flow provides a plausible basis for conserving seismic moment on long (centennial to millenary) time scales. Furthermore, this mechanism exhibits two additional characteristics that have been inferred from (paleo) seismological studies: First, T-instabilities have been observed in the simulations to occur both on seismically active and quiet faults, in agreement with natural observations from, for example, the regions of Cascadia, Andaman, Japan Trench, and Sumatra (Goldfinger et al., 2012; Ide, 2013; Satake, 2015). Second, the observed T-instabilities do not occur randomly in time, but instead recur quasi-periodically depending on the long-term rate of seismic moment accumulation and release, which has been speculated also for large natural earthquakes (Satake, 2015).

This interpretation now implies two different mechanisms for regular earthquakes and for giant earthquakes: The occurrence of the former is controlled by the size, spatial distribution, and rheological properties of (clusters of) asperities, which can be associated with competent lenses incorporated in tectonic mélanges (Fagereng, 2011b; Kimura et al., 2012). The frequency-magnitude distribution of regular earthquakes may follow from the asperity model proposed by Lay and Kanamori (1981), although in our simulations, a single seismological asperity corresponds to a cluster of competent lenses, rather than a discrete identifiable object. This class of earthquakes is familiar to previous numerical work employing rate-and-state friction. By contrast, model T-instabilities and natural giant earthquakes result from fault-averaged accumulation of seismic moment, and their dependence on the asperity distribution is only implicit through the seismic moment release by regular earthquakes, slow slip events, and creep. Lastly, large differences in the recurrence time of T-instabilities are observed in the simulations sharing similar statistical properties in the spatial and size distributions of asperities. It is presently unknown how stochastic noise expresses itself in simulations of higher dimensional faults, for example, whether or not statistically averaged behavior emerges controlled by rheological properties rather than asperity clustering and spacing. This topic deserves attention in future studies, particularly in estimating long-term seismic hazard and risk.

4.4. Forecasting and Precursors of Giant Earthquakes: Implications and Outlook

An important aspect of short-term forecasting of earthquakes is the presence (or absence) of slip transients, such as accelerated creep, foreshocks, and nonvolcanic tremor, associated with the nucleation phase of a seismic event. Numerous cases exist in which a main shock was preceded by geodetically detectable features (in hindsight Dodge et al., 1995; Jones & Molnar, 1979; Kanamori & Cipar, 1974; Kato et al., 2012, in hindsight), whereas other cases displayed no clear signs of an imminent event (Bakun et al., 2005; Irwan et al., 2004; Mellors, 2002). Hence, a fundamental understanding of the nucleation process may assist in interpreting this natural variability and in assessing the hazard associated with, for example, an emerging tremor swarm.

Previously, two models for earthquake nucleation have been put forward (Dodge et al., 1996; Ellsworth & Beroza, 1995): In the *preslip* model, a large seismic event nucleates from a region that grows largely independently of other, small slip events (e.g., foreshocks), which are carried by the expanding nucleation zone. Alternatively, the *cascade* model postulates that large events start out as an initially small event, which expands dynamically ("cascade up") by linking up with other nuclei until the rupture attains a size that satisfies the stability criterion exhibited by the larger event (the "break-away" phase). The preslip model permits a large, seismologically detectable preparation stage with accelerated creep preceding a large seismic event, which could aid in the early detection of an earthquake and estimation of its final size (Ellsworth & Beroza, 1995). Conversely, in the cascade model, it cannot a priori be established whether a small earthquake remains isolated or will ultimately cascade up to a much larger event.

In the simulations presented in this study, we observe clear examples of both end-member types of nucleation. On faults characterized by low D values, where (clusters of) asperities are sufficiently large to generate seismicity, P-instabilities appear to cascade up into T-instabilities (Figures 8a and 9a). Conversely, on faults characterized by high D values (which do not exhibit seismicity), the observed style of nucleation is best described by a preslip model (Figures 8c and 9c). However, in both scenarios, a T-instability only nucleates when the overall state of stress is sufficiently high (Figure 7). In other words, in both the cascade and preslip models, a T-instability only emerges when the fault is "ready." This view on nucleation is in complete agreement with previous interpretations of numerical simulations (Noda, Nakatani, et al., 2013) and laboratory experiments (McLaskey & Lockner, 2014).

Instead of focusing on the style of nucleation (which appears to be ambiguous), other characteristics of the fault rheology may be leveraged to aid seismic hazard assessment and forecasting. In seismological studies, it has been observed that tidal and seasonal forcing systematically affects tremor and slow slip patterns (Lambert et al., 2009; Pollitz et al., 2013; Rubinstein et al., 2008), from which it has been inferred that deep faults sections operate at extremely low friction (Houston, 2015), or near-lithostatic fluid pressure (Thomas et al., 2009). Analytical and numerical studies that have investigated the response of a fault subjected to periodic loading reveal that tremor activity rates are most sensitive to tidal modulation when $(a - b)$ is close to zero (Ader et al., 2012). An important characteristic of the nucleation process of a T-instability (and frictional instabilities in general) is the transition from velocity-strengthening ductile creep to velocity-weakening granular flow. Near the point of criticality, the velocity dependence of shear strength approaches neutrality; that is, $(a - b) \approx 0$. Provided that classical analyses of tidal modulation hold for CNS-governed fault rheologies, one can speculate on continuously probing the readiness of a fault based on its response to tide-induced tremor patterns. This warrants further investigation of the effect of tidal modulation on the behavior of heterogeneous faults. Another potential avenue for future investigation is the correlation between earthquake magnitudes and various fault zone parameters (such as plate velocity, temperature distribution, and fluid pressure), as to support statistical correlations with (micro)physical arguments (e.g., Heuret et al., 2011).

Lastly, we emphasize that the mechanism for generating T-instabilities (and equivalently giant earthquakes) facilitates the nucleation and propagation of dynamic ruptures on faults that creep aseismically (as is clearly seen in, e.g., Figure 4c). This implies that fault segments that exhibit low seismic coupling (i.e., that are not "locked") still carry substantial seismic hazard. As a prime example, the observation that no event in the historical M_w 6 Parkfield sequence ruptured the creeping section of the San Andreas fault does not preclude the possibility that this section ruptures in a future event, when the state of stress is sufficiently high.

5. Conclusions

This study considers the seismic cycle behavior of a spatially heterogeneous fault, of which the rheology is governed by a microphysical model formulation (Chen & Spiers, 2016; Niemeijer & Spiers, 2007). By using a microphysically based seismic cycle simulator (van den Ende, Chen, et al., 2018), the numerical modeling approach can be motivated and constrained directly by laboratory and field observations. From the analyses of heterogeneous faults, we conclude the following:

1. We observe that seismogenic asperities generate P-instabilities that are confined within fault regions exhibiting predominantly velocity-weakening behavior (nominal to the tectonic loading velocity).

Incremental slip in the asperities in the form of P-events, as well as far-field tectonic loading, may raise the stress supported by velocity-strengthening matrix fault segments. At a critical level of stress, an instability is triggered in the matrix, after which the entire fault ruptures in a single event (T-instability).

2. Heterogeneous faults exhibiting a random distribution in asperity size show a gradual increase in average stress, until the entire fault ruptures in a T-instability. T-instabilities are observed both in simulations that exhibit regular seismic events and in simulations that are seismically quiescent, highlighting a different underlying mechanism from regular earthquakes.
3. The occurrence of T-instabilities is facilitated by a transition from nondilatant, velocity-strengthening creep to dilatant, velocity-weakening granular flow. This transition is absent in classical rate-and-state friction formulations, but plays a central role in the stability of a heterogeneous fault that is governed by CNS microphysics (pressure solution and granular flow). Furthermore, it shows that fault materials characterized in laboratory tests as velocity-strengthening may still nucleate or facilitate unstable slip. In turn, this observation implies that creeping fault regions in nature are susceptible to seismic hazard.
4. We argue that the T-instabilities as seen in the simulations are analogous to great ($M_w > 8$) and giant ($M_w > 9$) megathrust earthquakes seen in nature. The consequences of the proposed mechanisms behind T-instabilities and giant earthquakes are in agreement with a number of (paleo)seismological observations, such as the occurrence of giant earthquakes in seismically quiet regions, their quasi-periodic recurrence, and possible violation of Gutenberg-Richter frequency-magnitude distributions based on regular earthquakes.
5. Ultimately, the occurrence of T-instabilities (and giant earthquakes) is driven by an accumulating slip deficit over the entire fault, resulting in an overall increase in stress and a transition from stable to unstable frictional sliding. This holds important implications for long-term seismic hazard assessments, as giant earthquakes can no longer be considered to result from purely stochastic origins, but instead are governed by seismic moment accumulation and release.

Appendix A: The Boundary Element Method

To model spatiotemporal variations of fault slip, we employ the boundary element code QDYN (Luo et al., 2017). This seismic cycle simulator originally utilizes rate-and-state friction to describe the model fault rheology, but it has been extended (van den Ende, Chen, et al. 2018) to include the CNS microphysical model as described above. Regardless of the underlying rheological model, the shear stress at point i on the fault is obtained using the quasi-dynamic approximation (Rice, 1993):

$$\tau_i(t) = -K_{ij}\left[d_j(t) - d_{imp}\right] - \eta V_i(t) \tag{A1}$$

Here, K_{ij} is a stress transfer kernel whose coefficients represent the shear stress induced on the ith fault element by unitary slip on the jth fault element, d_j is the total fault slip on the jth fault element, and d_{imp} is the far-field displacement, accumulating as $d_{imp} = V_{imp} \times t$. Radiation damping due to seismic wave radiation normal to the fault plane is accounted for by the last term on the right-hand side, in which the damping factor η assumes a value of $G/2c_s$, with G being the shear modulus of the homogeneous elastic medium, and c_s the shear wave speed (Rice, 1993). The stress transfer kernel K_{ij} is computed using a "2.5-D" approximation for infinite one-dimensional faults embedded in two-dimensional homogeneous media (see Luo & Ampuero, 2018), and fault stresses are obtained via the spectral approach in finite-size domains (Cochard & Rice, 1997). For numerical implementation, Equation A1 is differentiated with respect to time to give:

$$\frac{\mathrm{d}\tau_i}{\mathrm{d}t} = -K_{ij}\left[V_j(t) - V_{imp}\right] - \eta\frac{\mathrm{d}V_i(t)}{\mathrm{d}t} \tag{A2}$$

The fault slip velocity $V(t)$ is obtained as a function of stress and porosity as $V(\tau, \sigma, \phi) = h\left[\dot{\gamma}_{gr}(\tau, \sigma, \phi) + \dot{\gamma}_{ps}(\tau, \phi)\right]$. The acceleration term on right-hand side of Equation A2 is then decomposed in its partial derivatives as

$$\frac{dV}{dt} = \frac{\partial V d\tau}{\partial \tau\, dt} + \frac{\partial V d\phi}{\partial \phi\, dt} \tag{A3a}$$

$$\frac{\partial V}{\partial \tau} = h\left(A\frac{I_s\Omega}{dRT}f_1(\phi) + \dot{\gamma}_{gr}\left[\frac{1-\tilde{\mu}\tan\psi}{\tilde{a}(\sigma+\tau\tan\psi)}\right]\right) \tag{A3b}$$

$$\frac{\partial V}{\partial \phi} = h\left(\frac{\dot{\gamma}_{ps}}{\phi_c - \phi} + \dot{\gamma}_{gr}\left[\frac{2H(\sigma+\tilde{\mu}\tau)}{\tilde{a}(\sigma+\tau\tan\psi)}\right]\right) \tag{A3c}$$

Note that these partial derivatives are given specifically for the assumed porosity functions (Equation 2). Substitution of A3 into A2 and rearrangement give

$$\frac{d\tau_i}{dt} = \frac{-K_{ij}\left[V_j - V_{imp}\right] - \eta\frac{\partial V_i d\phi_i}{\partial \phi\ dt}}{1+\eta\frac{\partial V_i}{\partial \tau}} \tag{A4a}$$

$$\frac{d\phi_i}{dt} = -(1-\phi_i)\left(\dot{\varepsilon}_{gr,i} + \dot{\varepsilon}_{ps,i}\right) \tag{A4b}$$

These equations are of the general form $\dot{\mathbf{X}}=\mathbf{F}(\mathbf{X}, t)$, with $\mathbf{X}(t)$ being a vector containing the collection of $\tau_i(t)$ and $\phi_i(t)$ variables on all fault elements. This system of ordinary differential equations is solved by the fourth (fifth)-order Runge-Kutta-Fehlberg method with adaptive time stepping (Fehlberg, 1969; Shampine et al., 1976), as to maintain a relative error of $<10^{-5}$.

Appendix B: Rendering the Heterogeneous Fault Structure

By employing a microphysical model that contains microstructural information, one can closely relate the model fault geometry to field and laboratory observations. In this work, guided by numerous field reports, we define heterogeneity through spatial variations in pressure solution kinetics, which reflect contrasts in fault rock composition or spatial variations in strain rate. Following Fagereng (2011a), we assume that competent lenses (the asperities) obey a power-law distribution in size, that is:

$$F_X(x) = 1 - cx^{-D} \tag{B1}$$

where F_X is the cumulative size distribution of asperity size X, D is the fractal dimension (or power-law exponent), and c is a proportionality constant. Strictly speaking, this cumulative distribution function does not exist for $D > 0$ on an infinite domain (owing to the singularity at $x = 0$), but it can be redefined based on a rescaled probability density function integrated over a finite range of $0<x_{min} \le X \le x_{max}$ and $D\neq 0$, which yields

$$f'_X(x) = \frac{-Dx^{-D-1}}{x_{max}^{-D} - x_{min}^{-D}} \tag{B2a}$$

$$F'_X(x) = \int_{x_{min}}^{x} f'_X(x)dx = \frac{x^{-D} - x_{min}^{-D}}{x_{max}^{-D} - x_{min}^{-D}} \tag{B2b}$$

In accordance with the above relations, the realization of the asperity size distribution x can be generated from a uniform variate $\hat{X}$ as

$$x = \left(x_{min}^{-D} + \left[x_{max}^{-D} - x_{min}^{-D}\right]\hat{X}\right)^{-1/D} \tag{B3}$$

Even though the values of D reported by Fagereng (2011a) are based on measurements in a two-dimensional plane, they should similarly apply to a one-dimensional line (as assumed in this study) when the phacoids are equidimensional (i.e., unit aspect ratio, which is expected for the anti-plane cross section assumed here). When randomly transecting a two-dimensional plane with a given phacoid size distribution (characterized by their radius), all line intersections of the phacoids should scale by a factor $\pi/4 \approx 0.79$ of the radius (the

average chord length of an arbitrary intersection with a disk), and hence, the size distribution remains the same within a constant of order 1.

The procedure to render a fault with the desired statistical properties is then as follows:

1. First, the discrete asperity size distribution x_i is realized in accordance with Equation B3, with x_{min} corresponding to twice the fault element size and $x_{max} = L$. Between simulations, D is systematically varied between 1 and 2, following the phacoid fractal dimensions reported by Fagereng (2011a).
2. Next, a second size distribution (y_i) is realized that represents the spacing between neighboring asperities, assuming that the "gaps" between asperities obey the same power-law distribution.
3. In order to realize the desired asperity occupation ratio f, x_i is multiplied by $f/(1-f)$ (i.e., the ratio of total asperity length over total matrix length) before being combined in an arrangement with y_i.
4. The spatial distribution of Z_{ps} for the asperities and the matrix is then sampled from a piecewise alternating arrangement of x_i and y_i, respectively, where i ranges from 1 to N, so that $\sum_{i=1}^{N}(x_i + y_i) \geq L$. In other words, the spatial layout of the fault follows an arrangement $x_1, y_1, x_2, y_2, ..., x_N, y_N$.

Owing to the fault's finite size, stochastic noise causes some variability in the statistical properties of the fault geometry, for example, by randomly introducing one excessively large asperity, which skews the asperity size distribution. To prevent this, we compare each realized asperity size distribution with the expected distribution (Equation B2b) and the realized value of f with the one that is requested. For large (> 5%) deviations of the size distribution and f from the expected values, the rendered fault structure is rejected and a new one generated.

Appendix C: Lower Bounded Nucleation Length

Following Chen, Niemeijer, and Spiers (2017), we derive the CNS-equivalent rate-and-state friction parameters a, b, and D_c defined as

$$a \equiv \frac{\partial \mu}{\partial \ln V} \tag{C1a}$$

$$(a-b) \equiv \frac{\partial \mu_{ss}}{\partial \ln V} \tag{C1b}$$

$$D_c \equiv -V\frac{\partial \theta}{\partial \dot{\theta}} \tag{C1c}$$

In the granular flow regime (where a frictional instability may nucleate), the friction coefficient μ can be written as

$$\mu = \frac{\widetilde{\mu} + \tan\psi}{1 - \widetilde{\mu}\tan\psi} \tag{C2}$$

At steady-state, Equation 5b must equate to zero, so that

$$Z_{ps}\sigma f_2(\phi_{ss}) = \tan\psi_{ss}\dot{\gamma}_{gr} \approx \tan\psi_{ss}\frac{V_{ss}}{h} \tag{C3}$$

Correspondingly, μ_{ss} is found by substituting $V = V_{ss}$ and $\tan\psi = \tan\psi_{ss}$. The latter quantity follows from solving C3 for ϕ_{ss}:

$$\tan\psi_{ss} = 2H(\phi_c - \phi_{ss}) = \zeta\left[-1 + \sqrt{1 + 4H(\phi_c - \phi_0)\frac{1}{\zeta}}\right] \tag{C4}$$

with $\zeta \equiv hZ_{ps}\sigma/2V_{ss}$. We also recognize that, in the vicinity of steady-state, there exists a linear mapping between the porosity ϕ and state parameter θ (Chen, Niemeijer, & Spiers, 2017), which allows us to write

$$D_c \equiv -V\frac{\partial \theta}{\partial \dot{\theta}} = -V\frac{\partial \phi}{\partial \dot{\phi}} \tag{C5}$$

The CNS equivalent of a is trivially obtained by taking the partial derivative of Equation C2 with respect to V, which gives

$$a = \tilde{a}\frac{1+\tan^2\psi}{(1-\tilde{\mu}\tan\psi)^2} \tag{C6}$$

Similarly, $(a-b)$ is found by taking the partial derivative of Equation C2 with respect to V, substituting Equation C4for $\tan\psi$ (which then becomes an explicit function of V):

$$(a-b) = \frac{\tilde{a}+\frac{\partial\tan\psi_{ss}}{\partial\ln V}}{1-\tilde{\mu}\tan\psi_{ss}} + \frac{\tilde{\mu}+\tan\psi_{ss}}{(1-\tilde{\mu}\tan\psi_{ss})^2}\left(\tilde{\mu}\frac{\partial\tan\psi_{ss}}{\partial\ln V}+\tan\psi_{ss}\tilde{a}\right) \tag{C7}$$

with

$$\frac{\partial\tan\psi_{ss}}{\partial\ln V} = \frac{\partial\tan\psi_{ss}}{\partial\zeta}\frac{\partial\zeta}{\partial V}\frac{\partial V}{\partial\ln V} = -\tan\psi_{ss} + \frac{2H(\phi_c-\phi_0)\zeta}{\tan\psi_{ss}+\zeta} \tag{C8}$$

The equivalent value of b is then simply obtained by subtracting Equation C7 from Equation C6. Lastly, we find the CNS equivalent of D_c trough differentiation of Equation 5b with respect to ϕ and substituting the result in C5:

$$D_c = V\left[Z_{ps}\sigma\left(\frac{[\phi_c-\phi_0][1-\phi]}{[\phi_c-\phi]^2} - \frac{\phi-\phi_0}{\phi_c-\phi}\right) + 2H\frac{V}{h}(1-\phi)(\phi_c-\phi)\right]^{-1} \tag{C9}$$

With these results, we are able to compute an equivalent nucleation length L_{nucl} for a homogeneous fault as (Ampuero & Rubin, 2008):

$$L_{nucl} = \frac{1}{2}\frac{D_c G}{(b-a)\sigma} \tag{C10}$$

The minimum value of $L_{nucl} = 23.2$ m is achieved at a steady-state loading rate of $V = 1.73\times10^{-10}\,\mathrm{m\,s^{-1}}$. Asperities larger than 23 m are thus able to self-nucleate instabilities without requiring a nucleus that traverses matrix patches to connect with other asperities on the fault. However, for the nucleation of T-instabilities on faults with nonuniform frictional properties (as in the present study), the characteristic length scale for nucleation is likely (much) larger than what is given by L_{nucl} for homogeneous faults (Dublanchet, 2018). The value of L_{nucl} calculated above therefore represents an absolute lower bound. Moreover, since the CNS-equivalent estimates of $(a-b)$ and D_c are velocity- and state-dependent, they only hold in the vicinity of steady-state or equivalently for infinitesimally small velocity perturbations. For an extended nucleation zone in which the local slip rate spans over several orders of magnitude, an integral formulation is likely more accurate.

Acknowledgments

The authors thank two anonymous reviewers and the associate editor A. A. Gabriel for their thoughtful comments on the manuscript. M. v. d. E. thanks Å. Fagereng for sharing his views on fault zone structure. This project is supported by the European Research Council (ERC), Grant 335915, by the NWO Vidi-Grant 854.12.001 awarded to A. R. Niemeijer, and by the French government through the UCA^{JEDI} Investments in the Future project managed by the National Research Agency (ANR) with the referencenumber ANR-15-IDEX-01. J. P. A. acknowledges supplemental funding to NSF CAREER Grant EAR-1151926 for research opportunities in Europe.

Data Availability Statement

The most recent version of the QDYN source code is publicly available at https://github.com/ydluo/qdyn; an archived version is available at https://doi.org/10.5281/zenodo.322459.

References

Ader, T. J., Ampuero, J. P., & Avouac, J. P. (2012). The role of velocity-neutral creep on the modulation of tectonic tremor activity by periodic loading. *Geophysical Research Letters*, *39*, L16310. https://doi.org/10.1029/2012GL052326

Ampuero, J. P., & Rubin, A. M. (2008). Earthquake nucleation on rate and state faults—Aging and slip laws. *Journal of Geophysical Research*, *113*, B01302. https://doi.org/10.1029/2007JB005082

Atkinson, B. K. (1984). Subcritical crack growth in geological materials. *Journal of Geophysical Research*, *89*(B6), 4077–4114. https://doi.org/10.1029/JB089iB06p04077

Bakun, W. H., Aagaard, B., Dost, B., Ellsworth, W. L., Hardebeck, J. L., Harris, R. A., et al. (2005). Implications for prediction and hazard assessment from the 2004 Parkfield earthquake. *Nature*, *437*(7061), 969–974. https://doi.org/10.1038/nature04067

Bécel, A., Shillington, D. J., Delescluse, M., Nedimović, M. R., Abers, G. A., Saffer, D. M., et al. (2017). Tsunamigenic structures in a creeping section of the Alaska subduction zone. *Nature Geoscience*, *10*(8), 609–613. https://doi.org/10.1038/ngeo2990

Beeler, N. M., Tullis, T. E., Blanpied, M. L., & Weeks, J. D. (1996). Frictional behavior of large displacement experimental faults. *Journal of Geophysical Research*, *101*(B4), 8697–8715. https://doi.org/10.1029/96JB00411

Benedetti, L., Manighetti, I., Gaudemer, Y., Finkel, R., Malavieille, J., Pou, K., et al. (2013). Earthquake synchrony and clustering on Fucino faults (Central Italy) as revealed from in situ ^{36}Cl exposure dating. *Journal of Geophysical Research: Solid Earth*, *118*, 4948–4974. https://doi.org/10.1002/jgrb.50299

Bernabé, Y., & Evans, B. (2007). Numerical modelling of pressure solution deformation at axisymmetric asperities under normal load. *Geological Society, London, Special Publications*, *284*(1), 185–205. https://doi.org/10.1144/SP284.13

Bjorkum, P. A. (1996). How important is pressure in causing dissolution of quartz in sandstones? *Journal of Sedimentary Research*, *66*(1), 147–154. https://doi.org/10.1306/D42682DE-2B26-11D7-8648000102C1865D

Blanpied, M. L., Marone, C. J., Lockner, D. A., Byerlee, J. D., & King, D. P. (1998). Quantitative measure of the variation in fault rheology due to fluid-rock interactions. *Journal of Geophysical Research*, *103*(B5), 9691–9712. https://doi.org/10.1029/98JB00162

Bos, B., Peach, C. J., & Spiers, C. J. (2000). Frictional-viscous flow of simulated fault gouge caused by the combined effects of phyllosilicates and pressure solution. *Tectonophysics*, *327*(3), 173–194. https://doi.org/10.1016/S0040-1951(00)00168-2

Brantut, N., Heap, M., Meredith, P., & Baud, P. (2013). Time-dependent cracking and brittle creep in crustal rocks: A review. *Journal of Structural Geology*, *52*, 17–43. https://doi.org/10.1016/j.jsg.2013.03.007

Bullock, R. J., De Paola, N., Holdsworth, R. E., & Trabucho-Alexandre, J. (2014). Lithological controls on the deformation mechanisms operating within carbonate-hosted faults during the seismic cycle. *Journal of Structural Geology*, *58*, 22–42. https://doi.org/10.1016/j.jsg.2013.10.008

Bürgmann, R. (2005). Interseismic coupling and asperity distribution along the Kamchatka subduction zone. *Journal of Geophysical Research*, *110*, B07405. https://doi.org/10.1029/2005JB003648

Chen, J., & Niemeijer, A. R. (2017). Seismogenic potential of a gouge-filled fault and the criterion for its slip stability: Constraints from a microphysical model: Fault stability criterion. *Journal of Geophysical Research: Solid Earth*, *122*, 9658–9688. https://doi.org/10.1002/2017JB014228

Chen, J., Niemeijer, A. R., & Spiers, C. J. (2017). Microphysically derived expressions for rate-and-state friction parameters, a, b, and D_c: Microphysically derived RSF parameters. *Journal of Geophysical Research: Solid Earth*, *122*, 9627–9657. https://doi.org/10.1002/2017JB014226

Chen, J., & Spiers, C. J. (2016). Rate and state frictional and healing behavior of carbonate fault gouge explained using microphysical model. *Journal of Geophysical Research: Solid Earth*, *121*, 8642–8665. https://doi.org/10.1002/2016JB013470

Chester, F. M., Evans, J. P., & Biegel, R. L. (1993). Internal structure and weakening mechanisms of the San Andreas Fault. *Journal of Geophysical Research*, *98*(B1), 771–786. https://doi.org/10.1029/92JB01866

Chester, F., & Logan, J. (1987). Composite planar fabric of gouge from the Punchbowl Fault, California. *Journal of Structural Geology*, *9*(5-6), 621–IN6. https://doi.org/10.1016/0191-8141(87)90147-7

Cochard, A., & Rice, J. R. (1997). A spectral method for numerical elastodynamic fracture analysis without spatial replication of the rupture event. *Journal of the Mechanics and Physics of Solids*, *45*(8), 1393–1418. https://doi.org/10.1016/S0022-5096(97)00004-5

Collettini, C., Niemeijer, A., Viti, C., Smith, S. A., & Marone, C. (2011). Fault structure, frictional properties and mixed-mode fault slip behavior. *Earth and Planetary Science Letters*, *311*(3-4), 316–327. https://doi.org/10.1016/j.epsl.2011.09.020

De Paola, N., Collettini, C., Faulkner, D. R., & Trippetta, F. (2008). Fault zone architecture and deformation processes within evaporitic rocks in the upper crust. *Tectonics*, *27*, TC4017. https://doi.org/10.1029/2007TC002230

Dieterich, J. H. (1979). Modeling of rock friction: 1. Experimental results and constitutive equations. *Journal of Geophysical Research*, *84*(B5), 2161. https://doi.org/10.1029/JB084iB05p02161

Dodge, D. A., Beroza, G. C., & Ellsworth, W. L. (1995). Foreshock sequence of the 1992 Landers, California, earthquake and its implications for earthquake nucleation. *Journal of Geophysical Research*, *100*(B6), 9865–9880. https://doi.org/10.1029/95JB00871

Dodge, D. A., Beroza, G. C., & Ellsworth, W. L. (1996). Detailed observations of California foreshock sequences: Implications for the earthquake initiation process. *Journal of Geophysical Research*, *101*(B10), 22,371–22,392. https://doi.org/10.1029/96JB02269

Dove, P. M. (1999). The dissolution kinetics of quartz in aqueous mixed cation solutions. *Geochimica et Cosmochimica Acta*, *63*(22), 3715–3727. https://doi.org/10.1016/S0016-7037(99)00218-5

Dublanchet, P. (2018). The dynamics of earthquake precursors controlled by effective friction. *Geophysical Journal International*, *212*, 853–871. https://doi.org/10.1093/gji/ggx438

Dublanchet, P., Bernard, P., & Favreau, P. (2013). Interactions and triggering in a 3-D rate-and-state asperity model. *Journal of Geophysical Research: Solid Earth*, *118*, 2225–2245. https://doi.org/10.1002/jgrb.50187

Ellsworth, W. L., & Beroza, G. C. (1995). Seismic evidence for an earthquake nucleation phase. *Science, New Series*, *268*(5212), 851–855.

Fagereng, Å. (2011a). Frequency-size distribution of competent lenses in a block-in-matrix mélange: Imposed length scales of brittle deformation? *Journal of Geophysical Research*, *116*, B05302. https://doi.org/10.1029/2010JB007775

Fagereng, Å. (2011b). Geology of the seismogenic subduction thrust interface. *Geological Society, London, Special Publications*, *359*(1), 55–76. https://doi.org/10.1144/SP359.4

Faulkner, D., Jackson, C., Lunn, R., Schlische, R., Shipton, Z., Wibberley, C., & Withjack, M. (2010). A review of recent developments concerning the structure, mechanics and fluid flow properties of fault zones. *Journal of Structural Geology*, *32*(11), 1557–1575. https://doi.org/10.1016/j.jsg.2010.06.009

Faulkner, D., Lewis, A., & Rutter, E. (2003). On the internal structure and mechanics of large strike-slip fault zones: Field observations of the Carboneras fault in southeastern Spain. *Tectonophysics*, *367*(3-4), 235–251. https://doi.org/10.1016/S0040-1951(03)00134-3

Fehlberg, E. (1969). Low-order classical Runge-utta formulas with step-size control and their application to some heat-transfer problems. 315.

Fondriest, M., Smith, S. A., Di Toro, G., Zampieri, D., & Mittempergher, S. (2012). Fault zone structure and seismic slip localization in dolostones, an example from the Southern Alps, Italy. *Journal of Structural Geology*, *45*, 52–67. https://doi.org/10.1016/j.jsg.2012.06.014

Goldfinger, C., Ikeda, Y., Yeats, R. S., & Ren, J. (2013). Superquakes and supercycles. *Seismological Research Letters*, *84*(1), 24–32. https://doi.org/10.1785/0220110135

Goldfinger, C., Nelson, C. H., Morey, A. E., Johnson, J. E., Patton, J. R., Karabanov, E., et al. (2012). Turbidite event history—Methods and implications for holocene paleoseismicity of the Cascadia subduction zone. U.S. Geological Survey Professional Paper, 1661-F, U.S. Geological Survey, https://pubs.usgs.gov/pp/pp1661f/

Gomberg, J. (2010). Slow-slip phenomena in Cascadia from 2007 and beyond: A review. *Geological Society of America Bulletin*, *122*(7-8), 963–978. https://doi.org/10.1130/B30287.1

Hadizadeh, J., Mittempergher, S., Gratier, J. P., Renard, F., Di Toro, G., Richard, J., & Babaie, H. A. (2012). A microstructural study of fault rocks from the SAFOD: Implications for the deformation mechanisms and strength of the creeping segment of the San Andreas Fault. *Journal of Structural Geology*, *42*, 246–260. https://doi.org/10.1016/j.jsg.2012.04.011

Heuret, A., Lallemand, S., Funiciello, F., Piromallo, C., & Faccenna, C. (2011). Physical characteristics of subduction interface type seismogenic zones revisited. *Geochemistry, Geophysics, Geosystems*, *12*, Q01004. https://doi.org/10.1029/2010GC003230

Hickman, S. H., & Evans, B. (1995). Kinetics of pressure solution at halite-silica interfaces and intergranular clay films. *Journal of Geophysical Research*, *100*(B7), 13,113–13,132. https://doi.org/10.1029/95JB00911

Holdsworth, R., van Diggelen, E., Spiers, C., de Bresser, J., Walker, R., & Bowen, L. (2011). Fault rocks from the SAFOD core samples: Implications for weakening at shallow depths along the San Andreas Fault, California. *Journal of Structural Geology*, *33*(2), 132–144. https://doi.org/10.1016/j.jsg.2010.11.010

Houston, H. (2015). Low friction and fault weakening revealed by rising sensitivity of tremor to tidal stress. *Nature Geoscience*, *8*(5), 409–415. https://doi.org/10.1038/ngeo2419

Ide, S. (2013). The proportionality between relative plate velocity and seismicity in subduction zones. *Nature Geoscience*, *6*(9), 780–784. https://doi.org/10.1038/ngeo1901

Iler, R. (1973). Effect of adsorbed alumina on the solubility of amorphous silica in water. *Journal of Colloid and Interface Science*, *43*(2), 399–408. https://doi.org/10.1016/0021-9797(73)90386-X

Irwan, M., Kimata, F., Hirahara, K., Sagiya, T., & Yamagiwa, A. (2004). Measuring ground deformations with 1-Hz GPS data: The 2003 Tokachi-oki earthquake (preliminary report). *Earth, Planets and Space*, *56*(3), 389–393. https://doi.org/10.1186/BF03353070

Jefferies, S., Holdsworth, R., Wibberley, C., Shimamoto, T., Spiers, C., Niemeijer, A., & Lloyd, G. (2006). The nature and importance of phyllonite development in crustal-scale fault cores: An example from the Median Tectonic Line, Japan. *Journal of Structural Geology*, *28*(2), 220–235. https://doi.org/10.1016/j.jsg.2005.10.008

Johnson, J. M., Satake, K., Holdahl, S. R., & Sauber, J. (1996). The 1964 Prince William Sound earthquake: Joint inversion of tsunami and geodetic data. *Journal of Geophysical Research*, *101*(B1), 523–532. https://doi.org/10.1029/95JB02806

Jones, L. M., & Molnar, P. (1979). Some characteristics of foreshocks and their possible relationship to earthquake prediction and premonitory slip on faults. *Journal of Geophysical Research*, *84*(B7), 3596–3608. https://doi.org/10.1029/JB084iB07p03596

Kagan, Y. Y. (1997). Seismic moment-frequency relation for shallow earthquakes: Regional comparison. *Journal of Geophysical Research*, *102*(B2), 2835–2852. https://doi.org/10.1029/96JB03386

Kagan, Y. Y., & Jackson, D. D. (2013). Tohoku earthquake: A surprise? *Bulletin of the Seismological Society of America*, *103*(2B), 1181–1194. https://doi.org/10.1785/0120120110

Kanamori, H., & Cipar, J. J. (1974). Focal process of the great Chilean earthquake May 22, 1960. *Physics of the Earth and Planetary Interiors*, *9*(2), 128–136. https://doi.org/10.1016/0031-9201(74)90029-6

Kaneko, Y., Avouac, J. P., & Lapusta, N. (2010). Towards inferring earthquake patterns from geodetic observations of interseismic coupling. *Nature Geoscience*, *3*(5), 363–369. https://doi.org/10.1038/ngeo843

Kato, A., Obara, K., Igarashi, T., Tsuruoka, H., Nakagawa, S., & Hirata, N. (2012). Propagation of slow slip leading up to the 2011 M_w 9.0 Tohoku-Oki earthquake. *Science*, *335*(6069), 705–708. https://doi.org/10.1126/science.1215141

Kimura, G., Yamaguchi, A., Hojo, M., Kitamura, Y., Kameda, J., Ujiie, K., et al. (2012). Tectonic mélange as fault rock of subduction plate boundary. *Tectonophysics*, *568-569*, 25–38. https://doi.org/10.1016/j.tecto.2011.08.025

Lambert, A., Kao, H., Rogers, G., & Courtier, N. (2009). Correlation of tremor activity with tidal stress in the northern Cascadia subduction zone. *Journal of Geophysical Research*, *114*, B00A08. https://doi.org/10.1029/2008JB006038

Lay, T., & Kanamori, H. (1981). An asperity model of large earthquake sequences. In D. W. Simpson, & P. G. Richards (Eds.), *Earthquake prediction: An international review* (Vol. 4, pp. 579–592). Washington, D. C.: American Geophysical Union. https://doi.org/10.1029/ME004p0579

Lay, T., Kanamori, H., Ammon, C. J., Nettles, M., Ward, S. N., Aster, R. C., et al. (2005). The great Sumatra-Andaman earthquake of 26 December 2004. *Science*, *308*, 1127–1133.

Lehner, F., & Leroy, Y. (2004). Sandstone compaction by intergranular pressure solution. https://doi.org/10.1016/S0074-6142(03)80019-0

Luo, Y., & Ampuero, J. P. (2018). Stability of faults with heterogeneous friction properties and effective normal stress. *Tectonophysics*, *733*, 257–272. https://doi.org/10.1016/j.tecto.2017.11.006

Luo, Y., Ampuero, J. P., Galvez, P., van den Ende, M., & Idini, B. (2017). QDYN: A quasi-dynamic earthquake simulator (v1.1). https://doi.org/10.5281/ZENODO.322459

Mannen, K., Yoong, K. H., Suzuki, S., Matsushima, Y., Ota, Y., Kain, C. L., & Goff, J. (2018). History of ancient megathrust earthquakes beneath metropolitan Tokyo inferred from coastal lowland deposits. *Sedimentary Geology*, *364*, 258–272. https://doi.org/10.1016/j.sedgeo.2017.11.014

Marone, C. (1998). Laboratory-derived friction laws and their application to seismic faulting. *Annual Review of Earth and Planetary Sciences*, *26*(1), 643–696. https://doi.org/10.1146/annurev.earth.26.1.643

Marzocchi, W., Sandri, L., Heuret, A., & Funiciello, F. (2016). Where giant earthquakes may come. *Journal of Geophysical Research: Solid Earth*, *121*, 7322–7336. https://doi.org/10.1002/2016JB013054

McCaffrey, R. (2008). Global frequency of magnitude 9 earthquakes. *Geology*, *36*(3), 263. https://doi.org/10.1130/G24402A.1

McLaskey, G. C., & Lockner, D. A. (2014). Preslip and cascade processes initiating laboratory stick slip. *Journal of Geophysical Research: Solid Earth*, *119*, 6323–6336. https://doi.org/10.1002/2014JB011220

Mellors, R. J. (2002). Lack of precursory slip to the 1999 hector mine, California, earthquake as constrained by InSAR. *Bulletin of the Seismological Society of America*, *92*(4), 1443–1449. https://doi.org/10.1785/0120010244

Niemeijer, A. R., & Collettini, C. (2014). Frictional properties of a low-angle normal fault under in situ conditions: Thermally-activated velocity weakening. *Pure and Applied Geophysics*, *171*(10), 2641–2664. https://doi.org/10.1007/s00024-013-0759-6

Niemeijer, A., & Spiers, C. (2006). Velocity dependence of strength and healing behaviour in simulated phyllosilicate-bearing fault gouge. *Tectonophysics*, *427*(1-4), 231–253. https://doi.org/10.1016/j.tecto.2006.03.048

Niemeijer, A. R., & Spiers, C. J. (2007). A microphysical model for strong velocity weakening in phyllosilicate-bearing fault gouges. *Journal of Geophysical Research*, *112*, B10405. https://doi.org/10.1029/2007JB005008

Niemeijer, A., Spiers, C., & Bos, B. (2002). Compaction creep of quartz sand at 400–600°C: Experimental evidence for dissolution-controlled pressure solution. *Earth and Planetary Science Letters*, *195*(3-4), 261–275. https://doi.org/10.1016/S0012-821X(01)00593-3

Noda, H., & Lapusta, N. (2013). Stable creeping fault segments can become destructive as a result of dynamic weakening. *Nature*, *493*(7433), 518–521. https://doi.org/10.1038/nature11703

Noda, H., Nakatani, M., & Hori, T. (2013). Large nucleation before large earthquakes is sometimes skipped due to cascade-up—Implications from a rate and state simulation of faults with hierarchical asperities. *Journal of Geophysical Research: Solid Earth*, *118*, 2924–2952. https://doi.org/10.1002/jgrb.50211

Ohta, Y., Freymueller, J., Hreinsdottir, S., & Suito, H. (2006). A large slow slip event and the depth of the seismogenic zone in the south central Alaska subduction zone. *Earth and Planetary Science Letters*, *247*(1-2), 108–116. https://doi.org/10.1016/j.epsl.2006.05.013

Paterson, M. S. (1995). A theory for granular flow accommodated by material transfer via an intergranular fluid. *Tectonophysics*, *245*(3), 135–151. https://doi.org/10.1016/0040-1951(94)00231-W

Philibosian, B., Sieh, K., Avouac, J. P., Natawidjaja, D. H., Chiang, H. W., Wu, C. C., et al. (2017). Earthquake supercycles on the Mentawai segment of the Sunda megathrust in the seventeenth century and earlier: Sunda Megathrust Earthquake Supercycles. *Journal of Geophysical Research: Solid Earth*, *122*, 642–676. https://doi.org/10.1002/2016JB013560

Platt, J. D., Brantut, N., & Rice, J. R. (2015). Strain localization driven by thermal decomposition during seismic shear: Localization and thermal decomposition. *Journal of Geophysical Research: Solid Earth*, *120*, 4405–4433. https://doi.org/10.1002/2014JB011493

Platt, J. D., Rudnicki, J. W., & Rice, J. R. (2014). Stability and localization of rapid shear in fluid-saturated fault gouge: 2. Localized zone width and strength evolution. *Journal of Geophysical Research: Solid Earth*, *119*, 4334–4359. https://doi.org/10.1002/2013JB010711

Pluymakers, A. M. H., Peach, C. J., & Spiers, C. J. (2014). Diagenetic compaction experiments on simulated anhydrite fault gouge under static conditions. *Journal of Geophysical Research: Solid Earth*, *119*, 4123–4148. https://doi.org/10.1002/2014JB011073

Pollitz, F. F., Wech, A., Kao, H., & Bürgmann, R. (2013). Annual modulation of non-volcanic tremor in northern Cascadia. *Journal of Geophysical Research: Solid Earth*, *118*, 2445–2459. https://doi.org/10.1002/jgrb.50181

Ratzov, G., Cattaneo, A., Babonneau, N., Déverchère, J., Yelles, K., Bracene, R., & Courboulex, F. (2015). Holocene turbidites record earthquake supercycles at a slow-rate plate boundary. *Geology*, *43*(4), 331–334. https://doi.org/10.1130/G36170.1

Renard, F., Dysthe, D., Feder, J., Bjørlykke, K., & Jamtveit, B. (2001). Enhanced pressure solution creep rates induced by clay particles: Experimental evidence in salt aggregates. *Geophysical Research Letters*, *28*(7), 1295–1298. https://doi.org/10.1029/2000GL012394

Rice, J. R. (1993). Spatio-temporal complexity of slip on a fault. *Journal of Geophysical Research*, *98*(B6), 9885. https://doi.org/10.1029/93JB00191

Rimstidt, J. D. (2015). Rate equations for sodium catalyzed quartz dissolution. *Geochimica et Cosmochimica Acta*, *167*, 195–204. https://doi.org/10.1016/j.gca.2015.07.030

Rowe, C. D., Meneghini, F., & Moore, J. C. (2011). Textural record of the seismic cycle: Strain-rate variation in an ancient subduction thrust. *Geological Society, London, Special Publications*, *359*(1), 77–95. https://doi.org/10.1144/SP359.5

Rubinstein, J. L., La Rocca, M., Vidale, J. E., Creager, K. C., & Wech, A. G. (2008). Tidal modulation of nonvolcanic tremor. *Science*, *319*(5860), 186–189. https://doi.org/10.1126/science.1150558

Ruff, L., & Kanamori, H. (1980). Seismicity and the subduction process. *Physics of the Earth and Planetary Interiors*, *23*(3), 240–252. https://doi.org/10.1016/0031-9201(80)90117-X

Ruina, A. (1983). Slip instability and state variable friction laws. *Journal of Geophysical Research*, *88*(B12), 10,359–10,370. https://doi.org/10.1029/JB088iB12p10359

Satake, K. (2015). Geological and historical evidence of irregular recurrent earthquakes in Japan. *Philosophical Transactions of the Royal Society A: Mathematical, Physical and Engineering Sciences*, *373*(2053), 20140375. https://doi.org/10.1098/rsta.2014.0375

Satake, K., & Atwater, B. F. (2007). Long-term perspectives on giant earthquakes and tsunamis at subduction zones. *Annual Review of Earth and Planetary Sciences*, *35*(1), 349–374. https://doi.org/10.1146/annurev.earth.35.031306.140302

Satake, K., & Fujii, Y. (2014). Review: Source models of the 2011 Tohoku earthquake and long-term forecast of large earthquakes. *Journal of Disaster Research*, *9*(3), 272–280. https://doi.org/10.20965/jdr.2014.p0272

Scholz, C. H. (2019). *The mechanics of earthquakes and faulting* (3rd ed.). Cambridge: Cambridge University Press. https://doi.org/10.1017/9781316681473

Shampine, L. F., Watts, H. A., & Davenport, S. M. (1976). Solving nonstiff ordinary differential equations—The state of the art. *SIAM Review*, *18*(3), 376–411. https://doi.org/10.1137/1018075

Shimamoto, T. (1986). Transition between frictional slip and ductile flow for halite shear zones at room temperature. *Science*, *231*(4739), 711–714. https://doi.org/10.1126/science.231.4739.711

Shimamoto, T., & Noda, H. (2014). A friction to flow constitutive law and its application to a 2-D modeling of earthquakes. *Journal of Geophysical Research: Solid Earth*, *119*, 8089–8106. https://doi.org/10.1002/2014JB011170

Sieh, K., Natawidjaja, D. H., Meltzner, A. J., Shen, C. C., Cheng, H., Li, K. S., et al. (2008). Earthquake supercycles inferred from sea-level changes recorded in the corals of west sumatra. *Science*, *322*(5908), 1674–1678. https://doi.org/10.1126/science.1163589

Skarbek, R. M., Rempel, A. W., & Schmidt, D. A. (2012). Geologic heterogeneity can produce aseismic slip transients. *Geophysical Research Letters*, *39*, L21306. https://doi.org/10.1029/2012GL053762

Smeraglia, L., Bettucci, A., Billi, A., Carminati, E., Cavallo, A., Di Toro, G., et al. (2017). Microstructural evidence for seismic and aseismic slips along clay-bearing, carbonate faults. *Journal of Geophysical Research: Solid Earth*, *122*, 3895–3915. https://doi.org/10.1002/2017JB014042

Spiers, C. J., de Meer, S., Niemeijer, A. R., & Zhang, X. (2004). Kinetics of rock deformation by pressure solution and the role of thin aqueous films. In S. Nakashima (Ed.), *Physicochemistry of Thin Film Mater* (pp. 129–158). Tokyo: Universal Academy Press.

Stevens, V. L., & Avouac, J. P. (2016). Millenary $M_w > 9.0$ earthquakes required by geodetic strain in the Himalaya: $M_w > 9.0$ Earthquakes in the Himalaya. *Geophysical Research Letters*, *43*, 1118–1123. https://doi.org/10.1002/2015GL067336

Thomas, A. M., Nadeau, R. M., & Bürgmann, R. (2009). Tremor-tide correlations and near-lithostatic pore pressure on the deep San Andreas fault. *Nature*, *462*(7276), 1048–1051. https://doi.org/10.1038/nature08654

Tinti, E., Bizzarri, A., & Cocco, M. (2005). Modeling the dynamic rupture propagation on heterogeneous faults with rate- and state-dependent friction. *Annals of Geophysics*, *48*(2), 327–345. https://doi.org/10.4401/ag-3205

Tullis, T. E. (2007). Friction of rock at earthquake slip rates. 131–152.

van den Ende, M. P. A., Chen, J., Ampuero, J. P., & Niemeijer, A. R. (2018). A comparison between rate-and-state friction and micro-physical models, based on numerical simulations of fault slip. *Tectonophysics*, *733*, 273–295. https://doi.org/10.1016/j.tecto.2017.11.040

van den Ende, M. P. A., & Niemeijer, A. R. (2018). Time-dependent compaction as a mechanism for regular stick-slips. *Geophysical Research Letters*, *45*, 5959–5967. https://doi.org/10.1029/2018GL078103

van den Ende, M. P. A., Niemeijer, A. R., & Spiers, C. J. (2019). Influence of grain boundary structural evolution on pressure solution creep rates. *Journal of Geophysical Research: Solid Earth*, *124*, 10,210–10,230. https://doi.org/10.1029/2019JB017500

van der Marck, S. C. (1996). Network approach to void percolation in a pack of unequal spheres. *Physical Review Letters*, *77*(9), 1785–1788. https://doi.org/10.1103/PhysRevLett.77.1785

Verberne, B. A., Chen, J., Niemeijer, A. R., de Bresser, J. H. P., Pennock, G. M., Drury, M. R., & Spiers, C. J. (2017). Microscale cavitation as a mechanism for nucleating earthquakes at the base of the seismogenic zone. *Nature Communications*, *8*(1), 1645. https://doi.org/10.1038/s41467-017-01843-3

Weng, H., & Yang, H. (2017). Seismogenic width controls aspect ratios of earthquake ruptures: Seismogenic width controls aspect ratios. *Geophysical Research Letters*, *44*, 2725–2732. https://doi.org/10.1002/2016GL072168

Witter, R. C., Carver, G. A., Briggs, R. W., Gelfenbaum, G., Koehler, R. D., La Selle, S., et al. (2016). Unusually large tsunamis frequent a currently creeping part of the Aleutian megathrust. *Geophysical Research Letters*, *43*, 76–84. https://doi.org/10.1002/2015GL066083

Yabe, S., & Ide, S. (2017). Slip-behavior transitions of a heterogeneous linear fault:. *Journal of Geophysical Research: Solid Earth*, *122*, 387–410. https://doi.org/10.1002/2016JB013132